





RESEARCH ARTICLE | JUNE 21 2024

Detached eddy simulation of the interaction between acoustics and flame dynamics during the transition before and after longitudinal thermoacoustic instability in a multi-element liquid rocket engine

Yuanzhe Liu (刘远哲) ; Zhuopu Wang (王琢璞)  ; Wen Ao (敖文) ; Yu Guan (关昱) ; Peijin Liu (刘佩进) 



Physics of Fluids 36, 065150 (2024)

<https://doi.org/10.1063/5.0212762>



Articles You May Be Interested In

Interaction between acoustics and flame dynamics in a multi-element liquid rocket engine: Mode switching via quasi-periodic oscillation

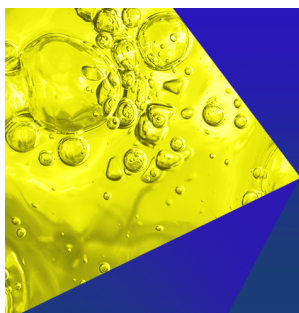
Physics of Fluids (February 2025)

Large eddy simulation of effects of oxidizer inlet temperatures on the transition routes before and after thermoacoustic instability in a subcritical hydrogen peroxide/kerosene liquid rocket engine

Physics of Fluids (December 2023)

Investigation of injector-coupled combustion dynamics in a methane–oxygen combustor using large eddy simulation and dynamic mode decomposition

Physics of Fluids (June 2024)



Physics of Fluids
Special Topics
Open for Submissions

[Learn More](#)

Detached eddy simulation of the interaction between acoustics and flame dynamics during the transition before and after longitudinal thermoacoustic instability in a multi-element liquid rocket engine

Cite as: Phys. Fluids **36**, 065150 (2024); doi: [10.1063/5.0212762](https://doi.org/10.1063/5.0212762)

Submitted: 6 April 2024 · Accepted: 3 June 2024 ·

Published Online: 21 June 2024



View Online



Export Citation



CrossMark

Yuanzhe Liu (刘远哲),¹ Zhuopu Wang (王琢璞),^{1,a)} Wen Ao (敖文),¹ Yu Guan (关昱),² and Peijin Liu (刘佩进)¹

AFFILIATIONS

¹Science and Technology on Combustion, Internal Flow and Thermal-structure Laboratory, Northwestern Polytechnical University, Xi'an 710072, China

²Department of Aeronautical and Aviation Engineering, The Hong Kong Polytechnic University, Kowloon, Hong Kong

^{a)}Author to whom correspondence should be addressed: zpwang@nwpu.edu.cn

ABSTRACT

In this study, we present the first numerical evidence of multiple bifurcation processes occurring in a multi-element model liquid rocket engine before and after the longitudinal thermoacoustic instability regime, as we vary the oxidizer inlet temperature within the range of 400–1400 K. To accurately capture the non-premixed turbulent combustion process, a comprehensive three-dimensional compressible detached eddy algorithm was employed, incorporating a two-step methane/oxygen chemical reaction kinetic mechanism based on OpenFOAM. After validating the numerical framework and achieving grid independence, we focus on (1) investigating the transition routes of system dynamics and (2) analyzing the spatiotemporal evolution of multiple jet combustion flow fields during the multi-bifurcation process. Our results indicate that the system dynamics undergoes two successive bifurcating processes. During the first bifurcation ($400\text{ K} \leq T \leq 800\text{ K}$), the system dynamics transitions into a full period-1 oscillation through intermittency. In the second bifurcation ($1200\text{ K} \leq T \leq 1400\text{ K}$), the system shifts from a limit cycle state back to a combustion noise state. The complex coupling mechanism between injectors is further elucidated through frequency spectrum results of radial velocity and temperature near the initial shear layer in the wakes of different injectors, especially the symmetry-breaking response between different injector jets. The analysis of snapshots and flame index also reveals the spatiotemporal evolution of combustion flow fields, specifically highlighting vortex dynamics, heat release, and combustion modes that potentially contribute to thermoacoustic instability.

Published under an exclusive license by AIP Publishing. <https://doi.org/10.1063/5.0212762>

I. INTRODUCTION

In recent decades, thermoacoustic instability has emerged as a significant risk to the development of liquid rocket engines, leading to degradation in engine performance and potential structural damage, ultimately resulting in catastrophic mission failures.¹ The presence of such instability is typically observed as high-amplitude and periodic pressure oscillations in the combustion chamber, resulting from the intricate interaction between flame heat release and the acoustic field.^{2,3} The acoustic actuator role is performed by the flame, while the combustion chamber acts as an acoustic resonator. If the heat release rate responds to acoustic fluctuations, a positive feedback loop is

established.⁴ Severe thermoacoustic instability was previously encountered in the development of the F-1 liquid rocket engine.⁵ Despite employing a “test-fail-test” approach, this issue was eventually resolved through the installation of baffles on the injector plate. However, challenges such as exorbitant costs and an elusive understanding of the underlying mechanism behind thermoacoustic instability have significantly captured the attention of engineers and researchers within the thermoacoustic community.

The occurrence of spontaneous oscillations in a thermoacoustic system indicates the presence of linear instability. In contrast, self-sustained periodic oscillation triggered by a finite amplitude stimulus

suggests conditional instability in an otherwise linearly stable system, which is due to the dominance of uncertain nonlinear mechanisms in the thermoacoustic system.⁶ In this paper, we focus on the spontaneous thermoacoustic instability, not the triggering instability. Despite decades of active research on this topic, the prediction of spontaneous thermoacoustic instability in real liquid rocket engines remains challenging. In conventional approaches, the thermoacoustic system is typically modeled as an acoustic system driven by an active flame, incorporating the interaction between flame and acoustics through a flame response function.⁷ Regarding the prediction tools for thermoacoustic instability, they are commonly categorized into linear frameworks and weak nonlinear approaches. The linear acoustic equation is utilized in the frequency domain for linear tools, in conjunction with the flame transfer function (FTF), to accurately anticipate the frequency and corresponding growth rate during the initiation of thermoacoustic instability.⁸ However, the linear method's disregard for nonlinear processes renders it incapable of accurately predicting the state of a limit cycle. The rocket and gas turbine communities have adopted different approaches to address weak nonlinear tools due to varying acoustic disturbance amplitudes in the combustion chamber. In rocket engines, the pressure disturbance amplitude in the combustion chamber is significantly high (20%–50%), leading to dominant nonlinear hydrodynamic effects within turbulent combustion systems.⁹ Conversely, gas turbines experience a relatively low-pressure disturbance of only 1%–5%, resulting in a weak nonlinear gas dynamics effect where the nonlinear flame response process takes precedence over other nonlinear mechanisms.¹⁰ Therefore, two types of methods, namely, the linear Euler's equation or linear Navier–Stokes equation combined with the flame transfer function (FTF) in the rocket community,¹¹ and the Helmholtz equation combined with flame describing function (FDF) in the gas turbine community, are employed to predict both the amplitude and frequency of limit cycles in spontaneous thermoacoustic instability.¹² The application of these methods has also yielded a series of achievements in the realm of industrial thermoacoustic systems.^{12–14}

In addition to advancing theoretical predictive tools within the thermoacoustic community, researchers are particularly interested in experimental measurements conducted on laboratory-scale engines. According to the unstable mode shape of the combustion chamber, thermoacoustic instability can be classified into longitudinal and transverse instability in liquid rocket engines. The German Aerospace Center (DLR) has extensively researched spontaneous transverse thermoacoustic instability through their associated experiment setup known as BKD, which involves a supercritical liquid rocket engine with 42 coaxial elements.¹⁵ William Anderson's team at Purdue University has developed a subcritical multi-element rectangular liquid rocket engine called TIC featuring a linear array of nine coaxial injectors to address the issue of spontaneous transverse thermoacoustic instability.¹⁶ It is widely recognized that the interaction between the injection system and the combustion chamber in liquid rocket engines with coaxial elements can lead to longitudinal thermoacoustic instability. Additionally, the team of Anderson has designed CVRC,^{9,17,18} a single-element liquid rocket combustor utilizing hydrogen peroxide and methane as propellants, and conducted experimental investigations on how different acoustic resonance lengths affect longitudinal thermoacoustic instability. The exceptional experimental measurements presented here establish a robust data foundation for the

advancement of theoretical prediction tools and high-fidelity numerical simulations in the field of thermoacoustic instability in coaxial-element liquid rocket engines.

However, the high temperature and pressure conditions in the engine operation environment limit the physical information that can be obtained through experimental measurement methods, making it difficult to achieve a comprehensive understanding of each combustion flow subsystem in rocket engines. To tackle this concern, high-fidelity numerical simulation techniques such as large eddy simulation (LES) or detached eddy simulation (DES) have recently assumed an increasingly pivotal role within the thermoacoustic community.^{1,19,20} The small-scale rocket engine BKD was investigated by Urbano *et al.*²¹ through a three-dimensional full-size LES study, revealing that the transverse thermoacoustic instability in the coaxial multi-element liquid rocket engine is primarily attributed to the coupling between the oxidizer injector and the combustion chamber. Guo *et al.*²² employed DES technology to simulate a rectangular rocket combustor and deduced that the transverse thermoacoustic instability arises from a positive feedback loop between perturbations in propellant mass flow rate and sudden heat release. Garby *et al.*²³ employed a compressible LES algorithm to elucidate the flame stabilization mechanism of CVRC as a triple flame and suggested that the axis-symmetric simulations can qualitatively replicate the instability characteristics of a single-element longitudinal rocket engine. The thermoacoustic instability of the CVRC configuration was simulated by Harvazinski *et al.*²⁴ using the DES algorithm, revealing that longitudinal instability is primarily caused by fuel flow disruption and reattachment during the acoustic oscillation. Nguyen and Sirignano²⁵ employed DES technology to substantiate that premixed combustion prevails as the predominant combustion mode under CVRC standard experimental conditions. High-fidelity numerical techniques enable researchers to shed some light on the underlying driving mechanisms of thermoacoustic instability; however, a significant knowledge gap exists in the literature regarding the transition to thermoacoustic instability in liquid rocket engines.

It is important to understand the evolution process of the pressure and the combustion flow subsystems under the control parameter space during the transition from the combustion noise state to the thermoacoustic instability state, because it may shed light on how the thermoacoustic instability arises. In the context of dynamical system theory, bifurcation refers to the qualitative alteration in system dynamics as control parameters vary. In thermoacoustic systems, it has been widely acknowledged hitherto that the system dynamics undergo a direct transition from the fixed point (combustion noise) to the limit cycle state (thermoacoustic instability), referred to as Hopf bifurcation.^{2,26,27} In the past decade, researchers have made significant advancements in thermoacoustic systems by incorporating dynamical systems theory, revealing the existence of nonlinear states beyond fixed points and limit cycle states, including quasi-periodic states,²⁸ intermittent behavior,^{29,30} period-*n* phenomena,³¹ and chaos.^{32,33} The limit cycle state represents only one potential state within the thermoacoustic system, rather than encompassing all possible end states. This finding challenges the conventional reduced-order predictive tools, which primarily focus on limit cycle states and exhibit limited effectiveness in capturing more intricate nonlinear states. Therefore, it is imperative for the thermoacoustic community to conduct comprehensive research on these intricate nonlinear states. The most

representative contributions to this field in liquid rocket engines were made by Sujith's group and Gotoda's group. Kasthuri *et al.*³⁴ observed that in the TIC rocket combustor, the system dynamics transitioned from combustion noise \rightarrow intermittency \rightarrow thermoacoustic instability as the Reynolds number of the oxidizer continuously varied. This finding suggests an alternative paradigm transitioning to thermoacoustic instability rather than relying solely on Hopf bifurcation. The presence of intermittency indicates the occurrence of thermoacoustic instability, which has also been demonstrated in other turbulent burners.^{35–37} Aoki *et al.*³⁸ conducted experimental measurements and employed nonlinear time series analysis methods to investigate the nonlinear characteristics of intermittent oscillation in a GH_2/GO_2 rocket burner under atmospheric pressure, which was devised to examine transverse thermoacoustic instability. In addition to employing dynamical systems theory tools for identifying paradigms transitioning into thermoacoustic instability, it is imperative to investigate the synchronization between the pressure and combustion flow subsystems. The thermoacoustic instability arises from the intricate interplay among hydrodynamics, unsteady combustion, and acoustic sub-processes within the combustion flow fields. This coupling between subsystems gives rise to self-organization and formation of dominant patterns in the combustion flow sub-systems.³⁹ In a coupled oscillating system, synchronization refers to the phenomenon of rhythm matching between oscillators. Hashimoto *et al.*⁴⁰ conducted numerical simulations to investigate the spatiotemporal dynamics of tangential thermoacoustic instability in GH_2/GO_2 rocket burners, considering atmospheric pressure conditions. Symbolic dynamics analysis was also performed by Shima *et al.*⁴¹ to examine the formation mechanism of transverse combustion instability. Kasthuri *et al.*^{42,43} focused on CH^* intensity and pressure signals from TIC rocket burners to analyze the transition from intermittent to thermoacoustic instability in terms of spatiotemporal dynamics. The findings indicated a shift in synchronization between pressure and heat release oscillations from desynchronization (DS) state to intermittent-phase synchronization (IPS) state prior to the onset of thermoacoustic instability.

The conventional perspective typically classifies the thermoacoustic stability of the combustion chamber into two states: combustion noise (fixed point) or thermoacoustic instability (limit cycle). However, experiments conducted on actual combustors have unveiled a plethora of intricate dynamical states beyond fixed point and limit cycle. These complex dynamical states often correspond to bifurcation behavior, signifying the transition from a state of combustion noise to a state of limit cycle. However, despite the pioneering efforts by Sujith's and Gotoda's groups, theoretical analysis, numerical simulation, and experimental measurement pertaining to unique engine structures, propellant types, and operating conditions in liquid rocket engines remain incomplete: (1) the identification of nonlinear states in liquid rocket engines is crucial for comprehending the progression of an engine from a state of combustion noise through a transitional route toward complete thermoacoustic instability. (2) Furthermore, the occurrence of combustion instability involves the simultaneous coupling between multiple subsystems of combustion flow and the acoustic field. It is widely accepted that thermoacoustic instability is caused by synchronicity. While a significant amount of literature on liquid rocket engines has focused on the dynamical behavior of combustion flow fields in thermoacoustic instabilities, limited knowledge exists regarding the synchronous dynamical behavior between the

acoustic field and the combustion flow subsystem during the transition from combustion noise state to limit cycle state. Understanding both the underlying mechanism of complex nonlinear states and its evolution within the combustion flow subsystem represents another major concern addressed in this paper. (3) Increasingly, a second bifurcation process has been observed in various thermoacoustic systems, potentially leading to the emergence of complex nonlinear states. The researchers discovered that within such a thermoacoustic system, as the control parameters continuously vary, the system dynamics transition from a state of combustion noise through the first bifurcation to reach a limit cycle state. Further changes in the control parameters may subsequently induce a second bifurcation, resulting in a transition from the limit cycle state to other nonlinear states. However, for liquid rocket engines, the second bifurcation process is rarely reported to our knowledge.

In order to address these issues, the multi-bifurcation processes occurring before and after the thermoacoustic instability regime are investigated in this paper using a complete three-dimensional detached eddy simulation in a multi-element model liquid rocket engine burning hydrogen peroxide/methane. The focus of this paper lies in the longitudinal thermoacoustic instability due to its potential coupling with the injection system, which has emerged as a prominent concern within the coaxial rocket community in recent years. In our previous research, we investigated the multiple bifurcation processes before and after the thermoacoustic instability regime in a single-element coaxial liquid rocket engine burning hydrogen peroxide and methane (or kerosene).^{29,30,44,45} In this study, we expand the computational domain to encompass multi-element liquid rocket engines and specifically investigate the interplay between injectors, thereby providing a valuable addition to the existing body of research. Given the catalytic decomposition of hydrogen peroxide with a mass concentration of 90%, resulting in the production of 58% water vapor and 42% oxygen at high temperature (1030 K) within the catalytic bed, uncertainties arise regarding the inlet conditions of the combustion chamber, particularly concerning the preheating temperature of the mixture comprising oxygen and water vapor and its potential impact on combustion instability. First, we investigate the transition of system dynamics to thermoacoustic instability during the first bifurcation within a parameter range of oxidizer inlet temperature ($400 \text{ K} \leq T \leq 800 \text{ K}$) in a multi-element liquid rocket engine. Additionally, we examine the frequency-dependent dynamics of jet vortex and flame in wakes generated by different injectors. Subsequently, in another parameter space where oxidizer inlet temperature ranges from 1200 to 1400 K, we explore the second bifurcation process: transitioning from a limit cycle state back to combustion noise in terms of system dynamics. Finally, through snapshot analysis and flame index analysis, we elucidate the temporal and spatial evolution of combustion flow field and combustion mode.

II. NUMERICAL FRAMEWORK

A. Governing equations and sub-grid models

The governing equations for the compressible turbulent reaction flow of a multi-species gas mixture are the Navier–Stokes equations, encompassing mass conservation, momentum conservation, energy conservation, and species transport. In detached (or large) eddy simulations, it is necessary to filter the complete Navier–Stokes equations. In this study, large-scale flows can be directly solved, while turbulence motions smaller than the filter scale can be mathematically modeled

using sub-grid turbulence models. According to the filtering operation, the variable $f(x, t)$ can be expressed as $f(x, t) \equiv \bar{f}(x, t) + \tilde{f}(x, t)$, where $\bar{f}(x, t)$ represents the filtered variable and $\tilde{f}(x, t)$ denotes the sub-grid scale variable. The Favre filtered Navier–Stokes equation can be further expressed as

$$\frac{\partial \bar{\rho}}{\partial t} + \frac{\partial \bar{\rho} \tilde{u}_j}{\partial x_j} = 0, \quad (1)$$

$$\frac{\partial \bar{\rho} \tilde{u}_j}{\partial t} + \frac{\partial (\bar{\rho} \tilde{u}_i \tilde{u}_j)}{\partial x_i} + \frac{\partial \bar{p}}{\partial x_j} = \frac{\partial (\tau_{ij} - \bar{\rho} (\tilde{u}_i \tilde{u}_j - \tilde{u}_i \tilde{u}_j))}{\partial x_i}, \quad (2)$$

$$\begin{aligned} \frac{\partial \bar{\rho} \tilde{h}_s}{\partial t} + \frac{\partial (\bar{\rho} \tilde{u}_i \tilde{h}_s)}{\partial x_i} &= \frac{D\bar{p}}{Dt} + \frac{\partial}{\partial x_i} \left[\lambda \frac{\partial \bar{T}}{\partial x_i} - \bar{\rho} (\tilde{u}_i \tilde{h}_s - \tilde{u}_i \tilde{h}_s) \right] \\ &+ \tau_{ij} \frac{\partial \tilde{u}_i}{\partial x_j} - \frac{\partial}{\partial x_i} \left(\rho \sum_{k=1}^N V_{k,i} Y_k h_{s,k} \right) + \bar{S}_{energy}, \end{aligned} \quad (3)$$

$$\begin{aligned} \frac{\partial (\bar{\rho} \tilde{Y}_k)}{\partial t} + \frac{\partial (\bar{\rho} \tilde{u}_i \tilde{Y}_k)}{\partial x_i} &= \frac{\partial}{\partial x_i} \left[\bar{V}_{k,i} \bar{Y}_k - \bar{\rho} (\tilde{u}_i \tilde{Y}_k - \tilde{u}_i \tilde{Y}_k) \right] + \bar{S}_{species}, \\ k &= 1, N. \end{aligned} \quad (4)$$

The variables ρ , u_j , p , h_s , and Y_k represent the density, velocity in the j -direction, pressure, enthalpy, and mass fraction of the species- k , respectively. τ_{ij} represents the stress tensor. \bar{S}_{energy} and $\bar{S}_{species}$ denote source terms due to chemical reactions. $V_{k,i} Y_k$ represents laminar diffusion flux. The stress tensor τ_{ij} of a gas mixture of multi-species can be expressed as

$$\tau_{ij} = -\mu \left(\frac{\partial u_i}{\partial x_j} + \frac{\partial u_j}{\partial x_i} - \frac{2}{3} \delta_{ij} \frac{\partial u_k}{\partial x_k} \right) - \mu_t \left(\frac{\partial u_i}{\partial x_j} + \frac{\partial u_j}{\partial x_i} - \frac{2}{3} \delta_{ij} \frac{\partial u_k}{\partial x_k} \right) + \tau_{ij}^{sgs}, \quad (5)$$

where μ represents the dynamic viscosity coefficient, μ_t represents the turbulent viscosity, δ_{ij} represents the Kronecker function, and τ_{ij}^{sgs} represents the sub-grid stress tensor. For diffusion flux, based on the Lewis number assumption of units ($Le = 1$), the mathematical expression is as follows:

$$\bar{V}_{k,i} \bar{Y}_k = -\bar{\rho} \bar{D}_k \frac{\partial \tilde{Y}_k}{\partial x_i}. \quad (6)$$

Among them, the \bar{D}_k represent the average molecular diffusion coefficient of species- k .

In the DES approach, the boundary layer utilizes unsteady RANS models, while separated regions are treated with LES. The LES region typically corresponds to the core turbulent area where large unsteady turbulence scales have a significant influence. Within this region, the DES models emulate sub-grid models similar to those used in LES. In the near-wall region, the respective RANS models are reinstated. DES models have been developed to tackle wall-bounded flows at high Reynolds numbers, where the expense of employing a near-wall resolving large eddy simulation would be expensive. The key distinction from the LES model lies in its reliance solely on the necessary RANS resolution within the boundary layers. Specifically, this paper uses DES technology combined with the SST $k-\omega$ model, and the specific mathematical expression can be referred to in Ref. 46. The partially stirred reactor (PaSR) model is implemented to deal with the interaction effect

between turbulence and chemical reaction, which has been done successfully with both turbulent premixed and non-premixed flames.^{47,48}

B. Numerical details

1. Physical models

The calculation configuration of this paper describes a model liquid rocket engine featuring multiple coaxial injection elements, as illustrated in Fig. 1(a). The study utilizes five coaxial injectors that are symmetrically distributed, with one injector positioned precisely at the geometric center of the cross section and the remaining four injectors equidistantly spaced around it. The coaxial injector operates in a shear mode where the gas oxidizer post is centrally located, and the gaseous fuel enters through the outer ring. The central oxidizer post has a length of 15 cm and a diameter of 2.05 cm, while the outer ring of the methane post measures 4 cm in length with a diameter of 2.3 cm. The inner annular seam spans 3 cm in length and has a diameter of 2.2 cm. A mixing section is present within the injector access for a distance of 1 cm before connecting to the combustion chamber, which itself measures 38.1 cm in length and has a diameter of 11.4 cm, maintaining an approximate cross-sectional area ratio to the nozzle throat at 5:1.

Figures 1(b) and 1(c) illustrate the grid distribution near the injector and short nozzle. To ensure mesh orthogonality, a block-structured hexahedral mesh element is generated within the three-dimensional computational domain of the multi-element rocket combustor. The turbulent mixing processes near the shear layer are accurately resolved by implementing local refinement, with a minimum mesh size smaller than 0.1 mm. This study presents a total of 9.2×10^6 hexahedral cells in the computation. Additionally, Sec. III A demonstrates three structured grids with varying resolutions to assess their impact on the computation results and verify grid independence.

Figure 2 shows a two-dimensional slice of the calculation area and a schematic diagram of the monitoring point setup. The locations of the monitoring points are, respectively, probe 1 (0, 0.056, and 0.01 m), probe 2 (0, 0.0115, and 0.01 m), probe 3 (0, 0.0455, and 0.01 m), probe 4 (0, -0.0455, and 0.01 m), probe 5 (0.0455, 0, and 0.01 m), and probe 6 (-0.0455, 0, and 0.01 m). Probe 1 is positioned adjacent to the combustion chamber wall, precisely at the antinode of the first-order acoustic mode within the combustion chamber. Probes

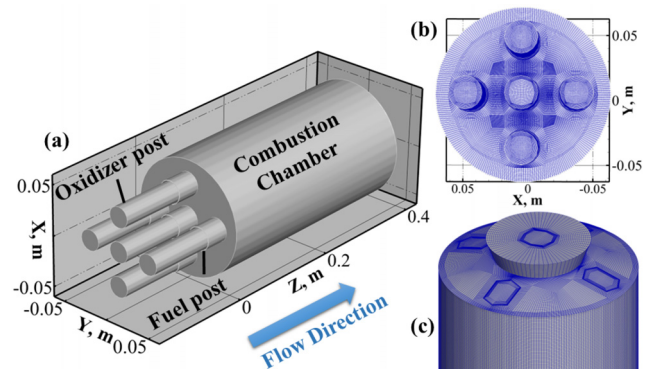


FIG. 1. (a) Three-dimensional calculation region of multi-element model rocket combustor. (b) A block-structured local grid near the injector. (c) A block-structured local grid near the nozzle.

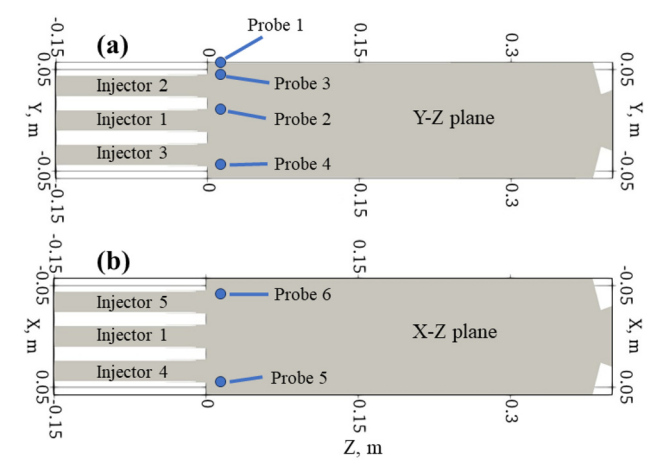


FIG. 2. Schematic diagram of 2D slices and monitoring points: (a) y–z plane and (b) the x–z plane.

2, 3, 4, 5, and 6 are located near the initial shear layer downstream of the five injectors, respectively, which is the region where fuel and oxidizer mix and burn. Due to the interaction of high-/low-speed flows, the vortex formed downstream of the dump plane will pass through this location during downward convection. Therefore, these five locations have been selected for monitoring the velocity and temperature in the combustion flow field, aiming to provide quantitative comparative results of the dynamic evolution process of combustion flow fields corresponding to different injectors.

2. The mechanism of chemical reaction kinetics

The present study employs hydrogen peroxide as an oxidizer and methane as a fuel. Specifically, a high-temperature catalytic bed is utilized to decompose a 90% mass concentration of hydrogen peroxide, resulting in the production of 42% oxygen and 58% water vapor. Subsequently, the resultant high-temperature oxidizer is introduced into the combustion chamber at 1030 K, where it undergoes turbulent mixing and combustion with methane. In this paper, a two-step methane/oxygen chemical reaction kinetic mechanism is employed. The specific parameter settings are described in Table 1. The chemical reaction mechanism incorporates six different species and follows a two-step process. In the first step, the chemical reaction kinetics are irreversible; however, in the second step, it becomes reversible leading to an equilibrium of combustion products CO and CO₂. This particular chemical reaction model was developed for turbulent flames involving methane/air mixtures and is widely employed for simulating combustion instability.^{49,50}

TABLE I. The mechanism of chemical reaction kinetics.

Chemical reactions	A, s ⁻¹	Ea, J/(kg* <i>mol</i>)	n_CH ₄	n_O ₂	n_CO ₂	n_CO
CH ₄ + 1.5O ₂ → CO + 2H ₂ O	2.0 × 10 ¹⁵	34 500	0.9	1.1		
CO + 0.5O ₂ ⇌ CO ₂	2.0 × 10 ⁹	12 000		0.5	1	1

TABLE II. Boundary conditions.

Part	Boundary condition	Value	Note
Oxidizer inlet	Mass flow rate	5 × 0.32 kg/s	Control parameter
	Temperature	400 K ≤ T ≤ 1400 K	
	Mass composition	42% O ₂ + 58% H ₂ O	
Methane inlet	Mass flow rate	5 × 0.027 kg/s	
	Temperature	300 K	
	Mass composition	100% CH ₄	
Walls	No-slip; non-permeable; and adiabatic		Supersonic outlet
	Wave transmissive	0.8 MPa	

3. Boundary conditions and initial conditions

The computational setup utilized in this study involves a model liquid rocket combustor equipped with five coaxial injection elements, designed to operate at a pressure of approximately 1.3 MPa. Hydrogen peroxide with a mass concentration of 90% was selected as the oxidizer and dissociated into 58% water vapor and 42% oxygen (by mass) through a high-temperature catalytic bed at 1030 K. Methane is employed as the fuel at an inlet temperature of 300 K, while maintaining total mass flow rates of fuel and oxidizer at 0.135 and 1.6 kg/s, respectively. The equivalence ratio of interest in this paper is oxidizer-rich conditions, specifically 0.8. Dirichlet boundary conditions are applied to both the oxidizer and fuel inlets for a constant mass flow rate. The outlet is equipped with wave-transmissive boundary conditions to effectively prevent the reflection of acoustic waves back into the combustion chamber, which is due to the supersonic velocities achieved by the nozzle outlet during operation. The walls are treated as non-slip, non-permeable adiabatic surfaces; zero gradient pressure boundary conditions apply to both rigid acoustic boundaries located upstream of oxidizer/fuel posts. In this paper, we are concerned with the dynamics of thermoacoustic system in the oxidizer inlet temperature parameter space. The specific boundary conditions are listed in Table II.

To establish the initial conditions, it is assumed that the combustion chamber is initially filled with high-temperature nitrogen (2000 K) at a static ambient pressure of 1.3 MPa. This approach facilitates ignition and expedites the attainment of the desired engine design pressure, thereby optimizing computational resources.

C. Numerical procedure

In this study, we utilized the open-source computational fluid dynamics software OpenFOAM to conduct a comprehensive three-dimensional compressible detached eddy simulation algorithm. To

simulate the turbulent reaction flow, we employed a modified version of the reactingFoam solver,⁵¹ widely recognized for its application in turbulent combustion studies encompassing both premixed and non-premixed combustion.^{52,53} The Favre-filtered Navier–Stokes equations, encompassing the mass equation, momentum equation, species transport equation, and energy equation were successfully solved. Furthermore, leveraging DES technology, we synergistically integrated the *SST k- ω* turbulence model with the *PaSR* turbulence combustion model to precisely simulate turbulent non-premixed gas phase combustion processes.

The working pressure of the combustion chamber was 1.3 MPa, which is lower than the critical pressure of methane and oxygen. Therefore, we employed the ideal gas equation of state to determine the density of the gaseous mixture. Based on previous literature,^{48,54} it was assumed that the gas phase mixture behaves ideally and adheres to Fickian diffusion law as well as Fourier heat conduction characteristics. The laminar viscosity was modeled using the Sutherland model. Simultaneously, we utilized the JANAF thermochemical table for calculating the specific heat values of each species.

The numerical program utilized the finite volume method (FVM) and a semi-implicit time integration scheme for unstructured meshes based on Gauss' theorem. Pressure-velocity coupling was achieved using the PIMPLE method, which combines elements of the SIMPLE algorithm and PISO algorithm, rendering it suitable for transient simulations. The discretization of the diffusion and convection terms employed a second-order central difference scheme, whereas the time integration was performed utilizing a Crank-Nicolson scheme with second-order accuracy.⁵³⁻⁵⁵ Each simulation case spanned a total physical time of 40 ms. To ensure accurate solutions across different time scales in turbulent combustion, a fine time step of 2×10^{-7} s was adopted for this study. Each case required approximately 16 640 CPU core hours operating at a clock speed of 2.4 GHz.

D. Verification of numerical framework

The numerical code used in this paper has been extensively validated in the previously published literature, including turbulent combustion instability and the ideal gas assumption.^{29,30,44,45,53} This section validates the numerical framework's capability to simulate combustion instability by utilizing a single-element model liquid rocket engine, known as CVRC, which was designed by Purdue University's research group and operates on hydrogen peroxide and methane propellants. The coaxial injector is gas-centered and shares the same geometric dimensions as those of a full-scale liquid rocket engine injector. The flow rate and operating conditions are set to mimic those of oxidizer-rich staged combustion (ORSC) cycles in full-scale rockets. Under controlled experimental conditions, hydrogen peroxide undergoes dissociation at a temperature of 1030 K within a high-temperature catalytic bed, resulting in the production of 42% oxygen and 58% water vapor (by mass) prior to entering the oxidizer post. Consequently, current numerical simulations of CVRC configurations and corresponding experimental conditions adopt an oxidizer inlet temperature of 1030 K. Methane enters the combustion chamber at room temperature through the fuel post. The setting of such working conditions is the same as that simulated in this paper, so CVRC was used for the numerical framework verification in this paper. Additionally, the experimental setup included a variable-length oxidizer post to investigate the impact of acoustic resonance on

self-excited longitudinal combustion instability. Experimental results demonstrate that as the length of the oxidizer post varies continuously from its shortest to longest configuration ($9\text{ cm} \leq L_{ox} \leq 19\text{ cm}$), gradual transitions can be observed in thermoacoustic stability, progressing from stable regions to unstable regions and ultimately returning to stable regions. In this section, the length of the oxidizer post was fixed at 14 cm to provide a comparison of the simulation results with the experimental measurements. For a more detailed introduction to the experimental equipment and operating conditions the reader is referred to the relevant literature.^{9,24,25,56}

Figure 3 shows the 3D CVRC geometry and the corresponding locally structured grid diagram. The verification example in this section utilized a hexahedral structured mesh generated in CVRC, comprising a total of 2.48×10^6 hexahedral cells. The combustion chamber was connected to an acoustically choked nozzle and a single coaxial injector. The length of the combustion chamber measured 38.1 cm, while the oxidizer post had a fixed length of 14 cm. The radius of the oxidizer post was 10.25 mm, the radius of the fuel post was 11.5 mm, and the radius of the combustion chamber was 22.5 mm. Additionally, the cross-sectional area ratio between the combustion chamber and nozzle throat was set at 5:1. To monitor variations in unsteady pressure, velocity, and temperature over time, two monitoring points were established: probe 1 (37, 0, and 2.2 cm) and probe 2 (1, 0, and 1 cm). Probe 1 was positioned at the end wall of the combustion chamber and corresponds to a probe located at an antinode within first-order acoustic mode; during CVRC experiments, a pressure sensor was installed downstream by approximately 37 cm from the dump plane to record pressure data accurately. Therefore, numerical monitoring focused on probe 1 to comprehend pressure evolution dynamics while probe 2 resided within the initial shear layer ($x/D_{\text{outer}} = 0.43$), where fuel and oxidizer were mixed.

Figure 4 shows the time series of pressure at monitoring point probe 1 and the time series of axial velocity and temperature at monitoring point probe 2. FFT analysis was used to analyze the spectrum results of oscillation signals. The periodic oscillations of high amplitude pressure, velocity, and temperature are shown in the figure, which

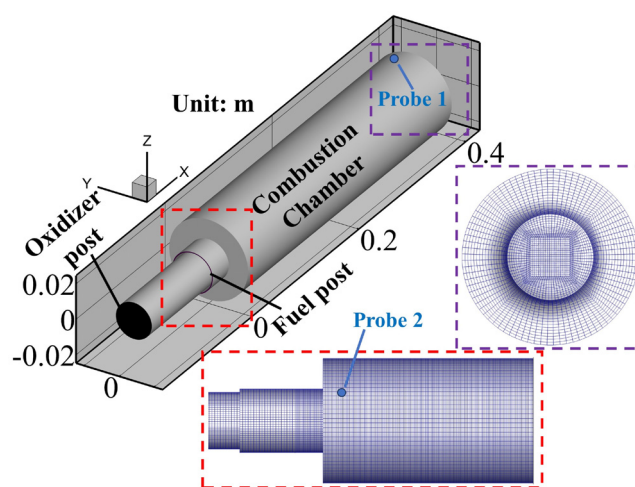


FIG. 3. A schematic overview: geometry of CVRC, the corresponding locally structured grid and the location of monitoring points probe 1 and probe 2.

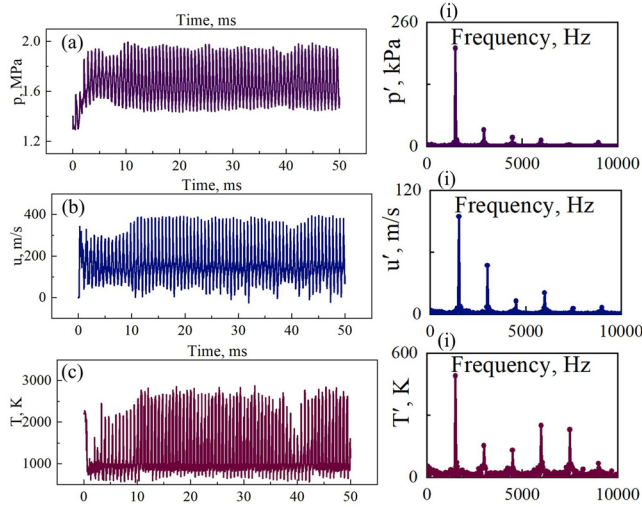


FIG. 4. (a) The time traces of pressure at the monitoring point probe 1, the time series of (b) axial velocity and (c) temperature at the monitoring point probe 2, and (i) the amplitude spectrum using the fast Fourier transform (FFT) algorithm.

is consistent with the limit cycle oscillations measured by CVRC experiments. The spectrum results also show several peaks, representing first-order, second-order, third-order, fourth-order, and fifth-order acoustic modes from left to right.

Table III quantitatively compares the first three acoustic modes with the experimental measurements in terms of oscillation frequency as well as the corresponding oscillation amplitude. (i) The numerical simulation results in this section reproduce the frequency doubling relationship between different acoustic modes. Both our calculation results and the simulation results in the literature²⁴ are higher than the experimental results, which can be attributed to the adiabatic treatment of the

combustion chamber wall. (ii) There is a very good agreement between the simulated oscillation peak-to-peak amplitude and the experimental measurement results, which means that the numerical simulation program in this paper can quantitatively reproduce the linear and nonlinear characteristics of the unstable combustion condition. In summary, the calculation program in this paper can quantitatively reproduce the thermo-acoustic instability of the liquid rocket engine with coaxial shear injector, which meets the needs of the subsequent calculation.

III. RESULTS AND DISCUSSION

A. Mesh details and validation

The present section compares three hexahedral grid elements with different resolutions, which are based on a block structure. Table IV presents the specific mesh size and distribution. As this paper primarily investigates longitudinal thermoacoustic instability, its primary characteristics manifest along the axial direction of the engine. Therefore, the three types of mesh size distributions are predominantly refined in the axial (z -axis) direction while remaining unchanged radially. The total number of hexahedral cell elements for these three meshes is 4.8×10^6 , 9.2×10^6 , and 13×10^6 , respectively.

The operating condition corresponds to the standard condition described in Sec. II B, wherein the oxidizer inlet temperature was maintained at 1030 K. Figure 5 depicts the system dynamics of pressure monitored at probe 1 using three different meshes. The results of three meshes exhibit the characteristic of period-1 thermoacoustic instability, which is qualitatively consistent with the experimental results.^{9,17,25,53} The pressure signal demonstrates that, after a brief development of the pressure disturbance, the system dynamics enter a state of limit cycle oscillation with constant amplitude and frequency. Subsequent FFT results reveal variations in both the oscillation frequency and amplitude among the three grid results. In mesh 1, the dominant frequency and corresponding normalized amplitude of the pressure oscillation were measured as 1513 Hz and 8.7%, respectively. For mesh 2, these values were observed to be 1538 Hz for the dominant

TABLE III. Comparison of the first three dominant acoustic modes.

Acoustic mode	Experiment ²⁴		DES results		Error		Harvazinski <i>et al.</i> ²⁴		Error	
	f , Hz	p'_{ptp} , kPa	f , Hz	p'_{ptp} , kPa	f	p'_{ptp}	f	p'_{ptp}	f	p'_{ptp}
1	1331	387	1500	411	12.7%	6.2%	1543	349	15.9%	9.8%
2	2655	89	2999	70	12.9%	21.3%	3114	87	17.3%	2.3%
3	3986	46	4499	38	12.8%	17.4%	4629	36	16.1%	21.8%

TABLE IV. Three-dimensional mesh size and distribution in multi-element liquid rocket combustor.

Mesh	Nodes $5 \times x \times y \times z$	Injector element				Nodes $x \times y \times z$	Combustion chamber				Cells (10^6)
		Length, mm					Length, mm				
		$(\Delta z)_{\min}$	$(\Delta z)_{\max}$	$(\Delta r)_{\min}$	$(\Delta r)_{\max}$		$(\Delta z)_{\min}$	$(\Delta z)_{\max}$	$(\Delta r)_{\min}$	$(\Delta r)_{\max}$	
1	$5 \times 61 \times 61 \times 78$	2	2	0.1	0.75	$130 \times 130 \times 220$	0.8	1.2	0.1	1.2	4.8
2	$5 \times 61 \times 61 \times 86$	1	2	0.1	0.75	$130 \times 130 \times 460$	0.5	1	0.1	1.2	9.2
3	$5 \times 61 \times 61 \times 86$	1	2	0.1	0.75	$130 \times 130 \times 750$	0.5	0.6	0.1	1.2	13

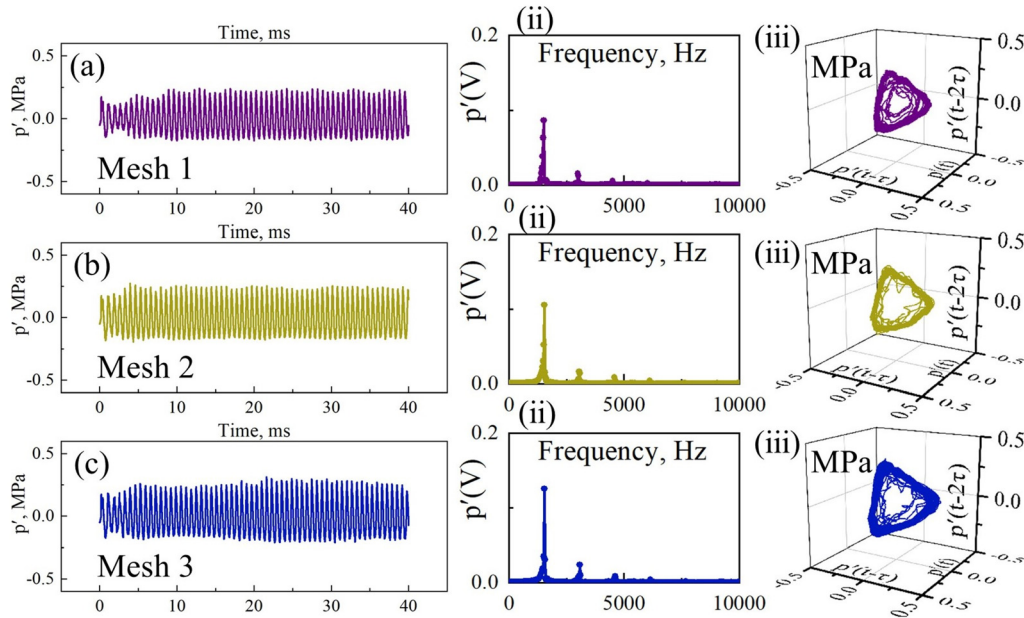


FIG. 5. The time series of pressure disturbance monitored at probe 1: (a) the normalized FFT results of mesh 1, (b) mesh 2, (c) mesh 3; (ii) and (iii) the phase diagram.

frequency and 10.6% for the peak value of pressure oscillation. In mesh 3, both the frequency and amplitude of pressure oscillation reached values of 1538 Hz and 12.6%, respectively. The similarity between the results of mesh 2 and mesh 3 is higher compared to that of mesh 1. Owing to the limited resolution of mesh 1, the predicted values for oscillation frequency and amplitude are underestimated. Despite slight differences observed in oscillation amplitudes between mesh 2 and mesh 3, their consistent instability frequencies indicate that mesh 2 effectively simulates the acoustic characteristics within the combustion chamber.

The spatial distribution of temperature and oxygen mass fraction after time averaging of the combustion field is illustrated in Fig. 6. The qualitative trend observed in the results of all three grid calculations remains consistent. However, mesh 2 exhibits minimal differences and acceptable errors compared to mesh 3 in terms of quantitative results. Conversely, the outcomes obtained from mesh 1 do not meet the calculation requirements adequately. Therefore, considering a balance between computational efficiency and accuracy, we have selected mesh 2 as the mesh for parametric research in this paper.

B. Intermittency route to limit cycle state

Before discussing the thermoacoustic instability, Fig. 7 illustrates the instantaneous spatial distribution characteristics of the combustion flow field at an oxidizer inlet temperature of 400 K. The engine profile exhibits the following characteristics: (i) Recirculation areas are observed between the downstream of two adjacent injectors, and between the downstream of the injectors and the wall of the combustion chamber, resulting in a negative axial velocity as shown in the black area in the image results. As the flow progresses downstream of the combustion chamber, multiple flow tube regions interact with each other in the wake of the oxidizer jet. However, near the dump plane,

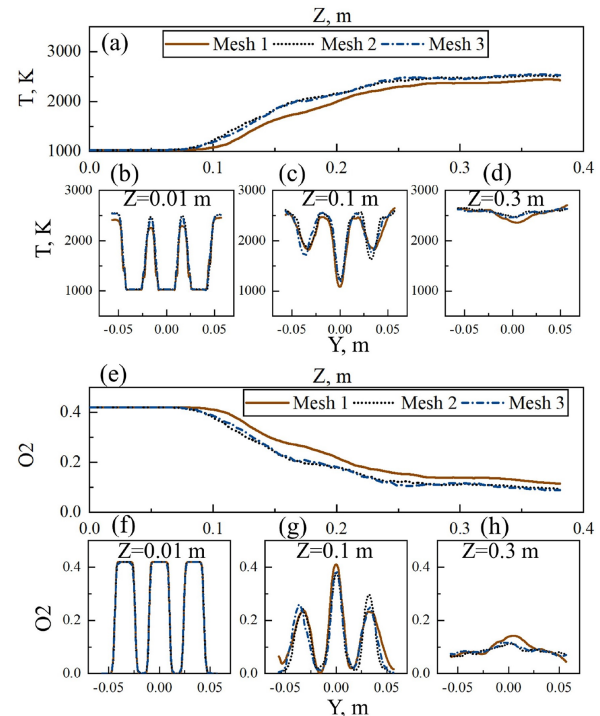


FIG. 6. Spatial distribution of temperature and oxygen mass fraction in the time average results: (a) and (e) axis of the combustion chamber ($x = 0$ m, $y = 0$ m, 0 m $\leq z \leq 0.381$ m); (b) and (f) diameter direction of the combustion chamber ($x = 0$ m, -0.05 m $\leq y \leq 0.05$ m, $z = 0.01$ m); (c) and (g) the diameter of the combustion chamber direction ($x = 0$ m, -0.05 m $\leq y \leq 0.05$ m, $z = 0.1$ m); and (d) and (h) the diameter of the combustion chamber ($x = 0$ m, -0.05 m $\leq y \leq 0.05$ m, $z = 0.3$ m).

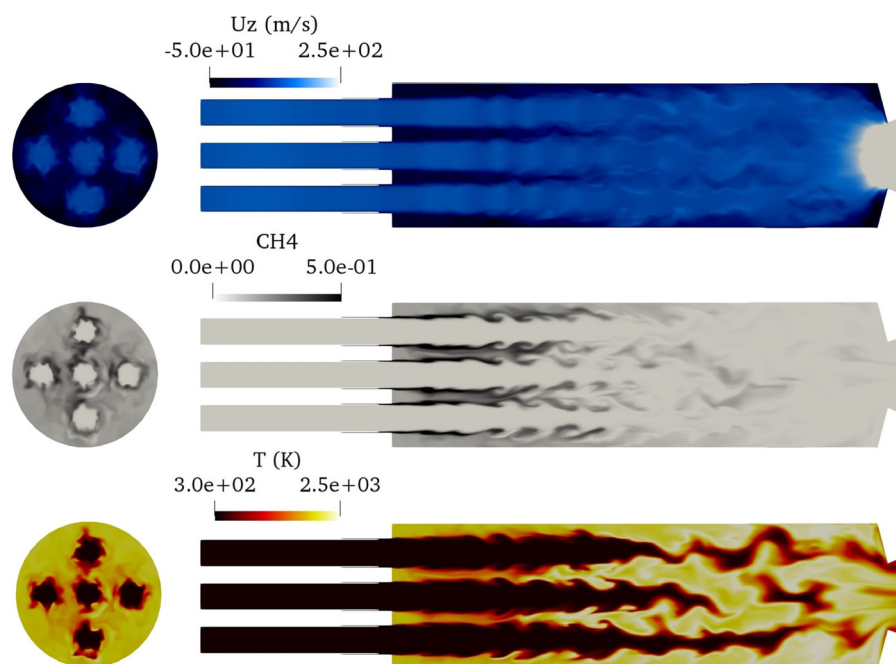


FIG. 7. Instantaneous spatial distribution of combustion flow field when the oxidizer inlet temperature is 400 K. Left: the cross section result of the combustion chamber when $z = 0.1$ m; right: y - z plane at $x = 0$ m; top: axial velocity results; middle: methane mass fraction results; bottom: temperature results.

velocity fields of oxidizer jets downstream of different injectors still exhibit relatively independent distribution characteristics. (ii) The distribution of methane mass fraction reveals the gradual growth and evolution of vortex structures, which transform into continuously distributed small-scale vortex structures during the downward development of methane jets. (iii) Spatial temperature distribution indicates that temperatures of combustion products near the dump plane are significantly lower than those generated downstream of the combustion chamber. This suggests that no significant flame was observed near the dump plane due to a substantial increase in ignition delay time caused by excessively low oxidizer inlet temperature; instead, flames were completely anchored by low-velocity hot products within recirculation zones.

The overview of system dynamics during the first bifurcation process under the parameter space of oxidizer inlet temperature ($400 \text{ K} \leq T \leq 800 \text{ K}$) is shown in Fig. 8. As the oxidizer inlet temperature increases, significant changes occur in the system dynamics evidenced by pressure traces, FFT results, and phase diagrams. Specifically, at lower temperatures ($400 \text{ K} \leq T \leq 500 \text{ K}$), the system exhibits intermittent oscillation. However, at higher temperatures ($600 \text{ K} \leq T \leq 800 \text{ K}$), it transitions into a period-1 limit cycle state. (1) Intermittency: When the combustion chamber temperature reaches $T = 400 \text{ K}$, low-amplitude periodic pressure oscillation initiates, transitioning into non-periodic oscillation after approximately 20 ms. This phenomenon can be effectively demonstrated through magnified time series and phase space trajectories. In the phase space trajectory, the state variable (i.e., pressure) gradually spirals inward from the periphery to the center during the initial calculation phase, ultimately converging into a low-amplitude limit cycle (represented by yellow and green state points). Over time, the phase space trajectory progressively invades the central region of phase space (depicted by blue state points). Spectrum analysis reveals that first-order sound waves (1205 Hz) dominate the pressure oscillation signal amidst wideband

combustion noise. A slight increase in oxidant inlet temperature ($T = 500 \text{ K}$) further enhances this intermittent pressure oscillation characteristic. The analysis of pressure time series demonstrates an initial increase followed by a subsequent decrease in amplitude over time; however, with further evolution, these oscillations are spontaneously amplified. The phase diagram exhibits more intriguing outcomes as initially, the motion path of the state variable (pressure) remains confined within a red single-loop structure; yet as amplitude increases, it forms a larger yellow single-loop structure (yellow state points). Subsequently, as amplitude begins to decay, the phase trajectory converges toward the center of phase space (represented by the green state point). Finally, with the continued passage of time, the trajectory of the state variable becomes restricted within a single-loop structure (the blue state point). (2) Period-1 limit cycle state: When the oxidizer inlet temperature is increased ($600 \text{ K} \leq T \leq 800 \text{ K}$), the system exhibits period-1 limit cycle oscillation, characterized by periodic oscillations with equal amplitude and frequency. This phenomenon can be observed through pressure time series, dominant peaks in FFT results, and single-loop structures in the embedding space. It should be emphasized that the amplitude of pressure at $T = 600 \text{ K}$ is significantly higher than that at $T = 800 \text{ K}$. As the amplitude of the pressure oscillation increases, there is a transfer of acoustic oscillation energy from the first-order acoustic frequency to the higher-order harmonics, resulting in more pronounced higher-order harmonic effects observed in FFT results.⁵⁷ The underlying physical mechanisms responsible for these intriguing variations will be subsequently elucidated.

The spatial distribution results of the spanwise vorticity in the y - z plane and the x - z plane are shown in Fig. 9(a), where the axial coordinate range is $-0.015 \text{ m} \leq z \leq 0.15 \text{ m}$. The results reveal an independent vortex evolution process with the smallest scale vortex structure observed near the dump plane in the wake of each injector element. As fluid convection occurs downward, energy is transferred

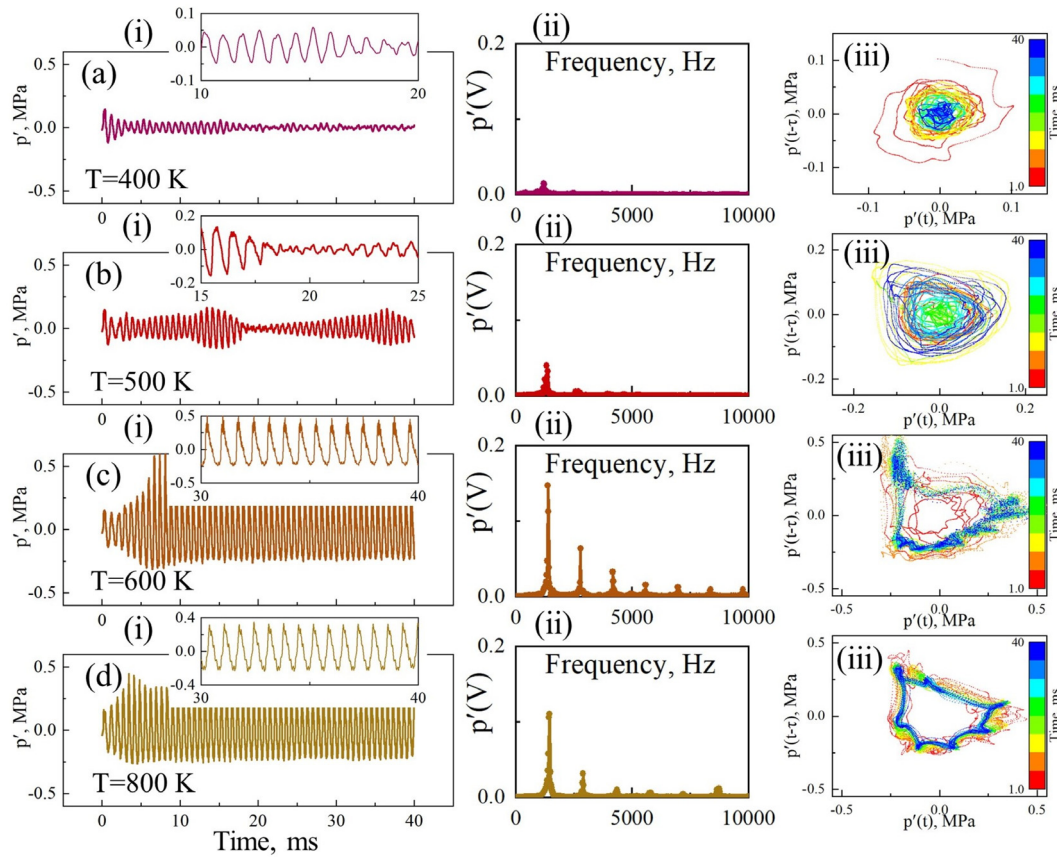


FIG. 8. Overview of system dynamics during the first bifurcation process under the parameter space of oxidizer inlet temperature: (a)–(d) the time series of pressure monitored at probe 1; (i) enlarged views of time series; (ii) FFT results normalized by $p'(V) = p'/\bar{p}$; and (iii) the phase space trajectory of the pressure, where the color bar shows the time evolution from 1 to 40 ms.

from the combustion flow field to enhance further growth of the vortex structure, leading to large-scale vortex structures appearing approximately 10 cm downstream of the dump plane. At this point, the wake of Injector No. 1 and its surrounding injector elements start interacting.

To quantitatively compare the evolution process of vortex dynamics in the wake of multi-injector, monitoring points probes 2–6 were strategically positioned near the initial shear layer. The vortex shedding frequency of Injectors No. 1–5, which can be identified as the peak frequency in the FFT analysis of their radial velocity oscillation, has been widely adopted and validated by numerous previous studies.^{29,45,58–60} Figure 9(b) shows the FFT results for the radial velocities in the wake of different injectors during the first bifurcation process. When $T = 400$ K, the FFT results of the radial velocity dynamics of all injector elements exhibit similar characteristics: dominant peaks are observed at 1205 and 4230 Hz, representing the first-order acoustic frequency and the intrinsic hydrodynamic instability frequency, respectively. Based on our previous discussions on a single-element rocket combustor,^{44,45,53} we attribute this reduction in the intrinsic hydrodynamic instability frequency (from 10 kHz to 4250 Hz) to a significant decrease in the velocity of the wake of the injector caused by lower oxidizer inlet temperatures. Furthermore, as discussed previously,^{44,45,53} it

can be inferred that this phenomenon arises from competition and cooperation between natural acoustic modes and intrinsic hydrodynamic modes during intermittent oscillation-induced vortex-shedding processes. In periodic pressure oscillations, natural acoustic modes dominate vortex shedding processes; however, in aperiodic pressure oscillations, intrinsic hydrodynamic instability processes take over. It is worth noting that differences in velocity amplitude also indicate a complex coupling process between the wakes of multi-injectors. At $T = 500$ K, analysis of natural acoustic characteristics reveals that five dominant peaks in the velocity spectrum represent the first five natural acoustic frequencies of the combustion chamber. Specifically, the dominant peak at Injector No. 1 corresponds to $f_5 = 6666 \text{ Hz} \approx 5 \times f_1 = 5 \times 1333 \text{ Hz}$, where f_5 represents the fifth acoustic frequency and f_1 represents the first acoustic frequency. The response of velocity spectrum for Injector No. 2 is similar to that of Injector No. 1. Vortex shedding frequencies for Injectors No. 3–5 were found to be $f_3 = 3948 \text{ Hz} \approx 3 \times f_1 = 3 \times 1333 \text{ Hz}$. Therefore, it can be inferred that at $T = 500$ K, the dominant frequency of vortex shedding for Injectors No. 1–2 is a fifth-order acoustic frequency and for Injectors No. 3–5, it is a third-order acoustic frequency. There is minimal disparity between the peaks corresponding to the first two dominant frequencies, indicating that vortex structures of varying sizes traverse

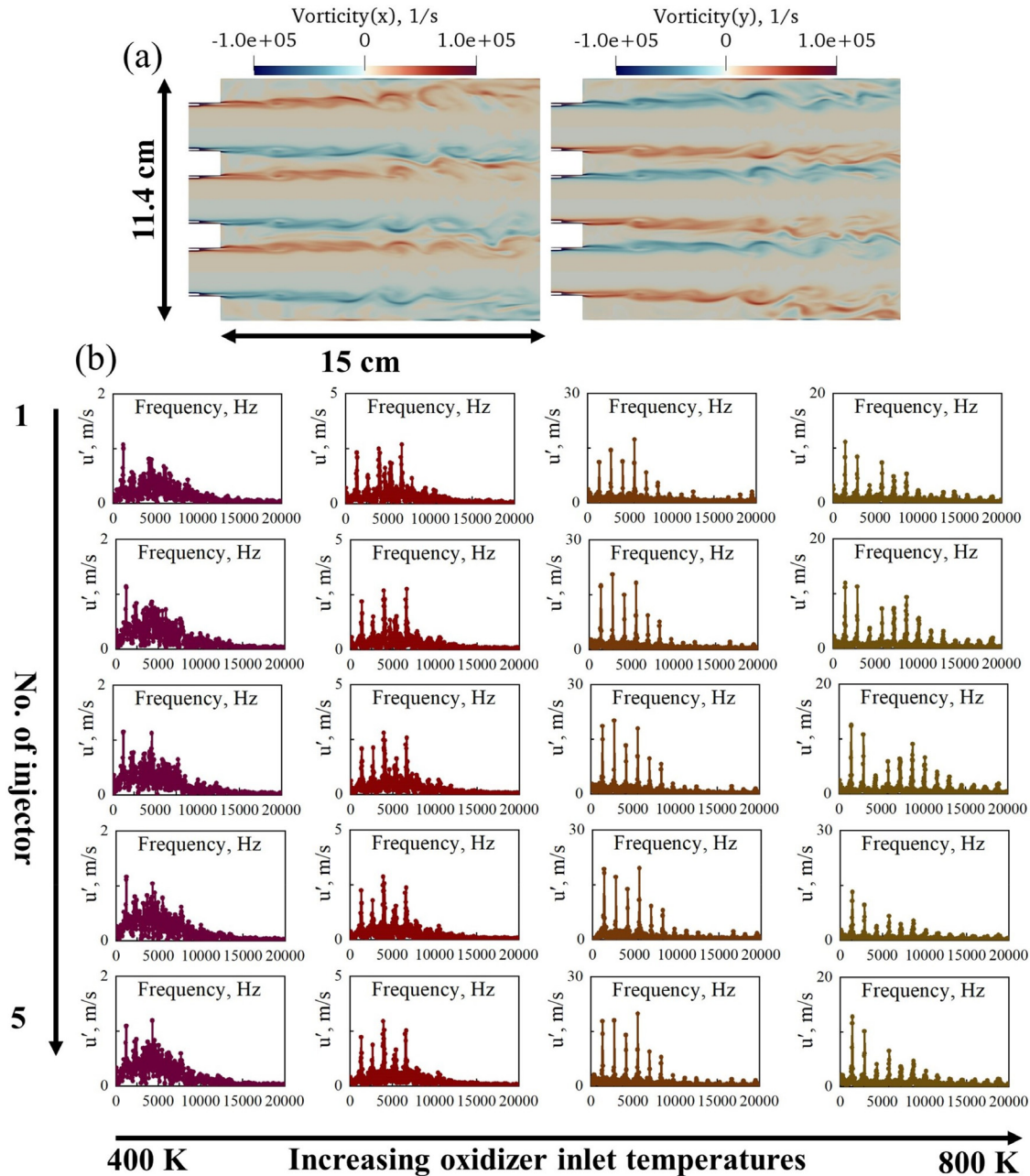


FIG. 9. (a) At $T = 400$ K, the instantaneous spatial distribution results of X-direction vorticity in the y - z plane and Y-direction vorticity in the x - z plane. (b) The FFT results of radial velocity signals monitored at probes 2, 3, 4, 5, and 6. The oxidizer inlet temperatures ranged from left to right: 400, 500, 600, and 800 K. The injectors are numbered as follows from top to bottom: Injector No. 1 to Injector No. 5.

through this location. The asymmetry in Injectors No. 2–5 jets can be attributed more plausibly to the stochastic nature of turbulent motion. As mentioned earlier, in intermittent cases, both acoustic oscillations and intrinsic hydrodynamic instability dominate system dynamics. Non-frequency synchronization relationship between injectors leads to complex system dynamics during intermittency. The symmetry-breaking

phenomenon⁶¹ in physics among injectors explains intermittent oscillation observed in liquid rocket engines.

For higher oxidizer inlet temperatures ($T = 600$ K), the velocity spectral response exhibits a distinct dominance of multiple peaks, which can be designated as f_1 – f_6 from left to right. The vortex shedding process of Injector No. 1, Injector No. 4, and Injector No. 5 is

primarily governed by f_4 , while the vortex shedding process of Injector No. 2 and Injector No. 3 is predominantly influenced by f_2 . Interestingly, in the intermittent case ($T = 500$ K), the injector's vortex shedding frequency corresponds to an odd high-order mode, whereas in the thermoacoustic instability range ($T = 600$ K), it aligns with an even order high-order mode. At $T = 800$ K, there is a slight reduction in pressure oscillation amplitude within the combustion chamber compared to $T = 600$ K. During this period, the dominant frequency for vortex shedding for all injectors becomes f_1 , indicating complete frequency-synchronization between them.

The frequency-synchronization results of the temperature fields at the initial shear layer in the wake of each injector during the first bifurcation are depicted in Fig. 10. Compared to the radial velocity results depicted in Fig. 9, the frequency response in the temperature field exhibits a straightforward distribution pattern. The spectral response of the temperature field shows that the first-order acoustic frequency (f_1) dominates. Specifically, at $T = 400$ K, the first dominant peak of the temperature response is still 1205 Hz, while the second dominant peak is 2435 Hz (f_2). The third dominant peak is 4333 Hz, which is close to the intrinsic hydrodynamic instability frequency (4230 Hz). The wideband noise around the intrinsic hydrodynamic instability mode is suppressed when the oxidizer inlet temperature

increases. The temperature and pressure oscillations are consistently found to be frequency-locked (f_1) during the initial bifurcation process.

C. Secondary Hopf bifurcations in rocket combustor

In Sec. II, we analyzed the spatiotemporal dynamics characteristics of the thermoacoustic system during its first bifurcation. It is pertinent to inquire whether a subsequent bifurcation phenomenon will occur in the system dynamics with further escalation of oxidizer inlet temperature. Figure 11 shows an overview of the system dynamics in the second bifurcation process ($1200 \text{ K} \leq T \leq 1400 \text{ K}$). When we continue to increase the oxidizer inlet temperature ($1200 \text{ K} \leq T \leq 1280 \text{ K}$), the system dynamics remain in a limit cycle state of period-1. Compared with the results in the thermoacoustic instability regime ($600 \text{ K} \leq T \leq 800 \text{ K}$) during the first bifurcation, although the spectral results of the pressure still show the dominance of first-order acoustic frequency, the amplitude of the pressure oscillation is further reduced. More interestingly, when the oxidizer inlet temperature is further increased ($1290 \text{ K} \leq T \leq 1400 \text{ K}$), the system dynamics show a qualitative shift, that is, the second bifurcation phenomenon. At $T = 1290 \text{ K}$, the pressure traces exhibit a transient period of oscillation lasting

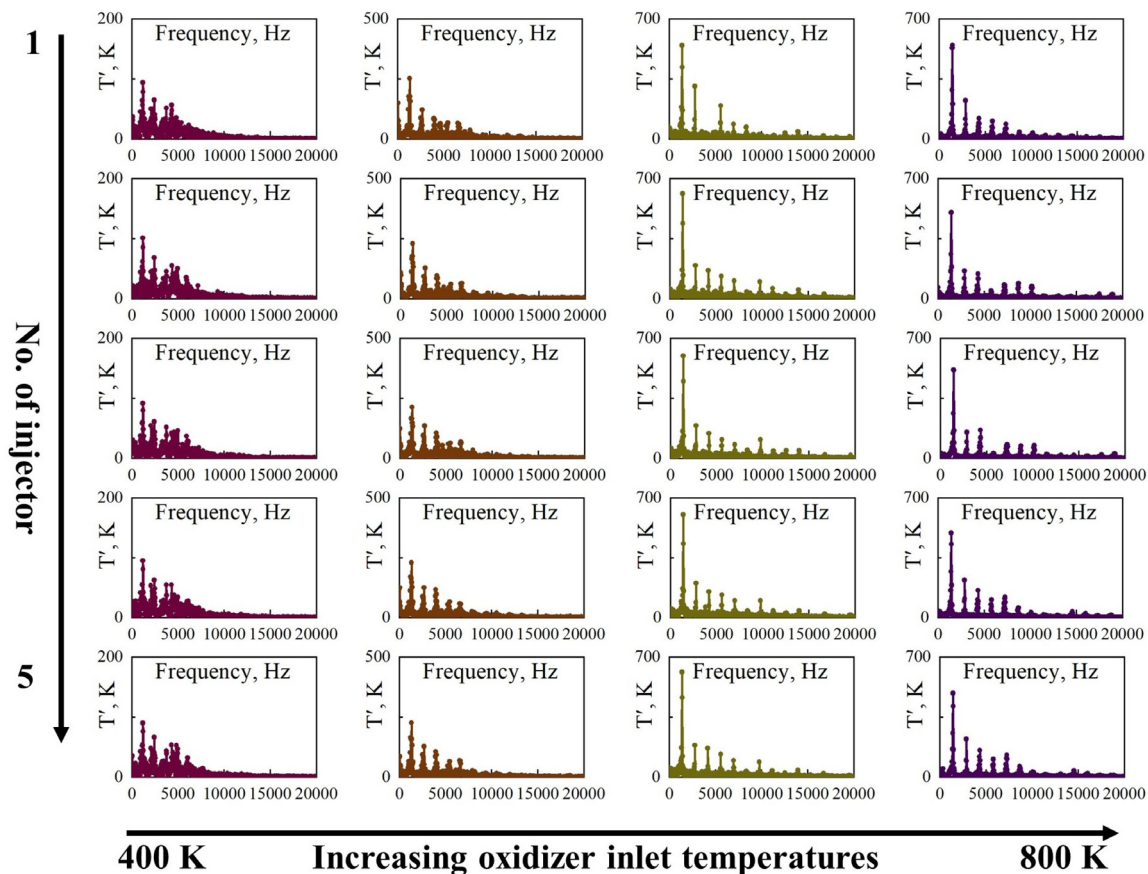


FIG. 10. The FFT results of the temperature signals monitored at probes 2, 3, 4, 5, and 6 are used to reveal the combustion process of Injectors No. 1, 2, 3, 4, and 5, respectively. FFT results from left to right represent the oxidizer inlet temperature of 400, 500, 600, and 800 K, respectively. Top to bottom: Injector No. 1 to Injector No. 5.

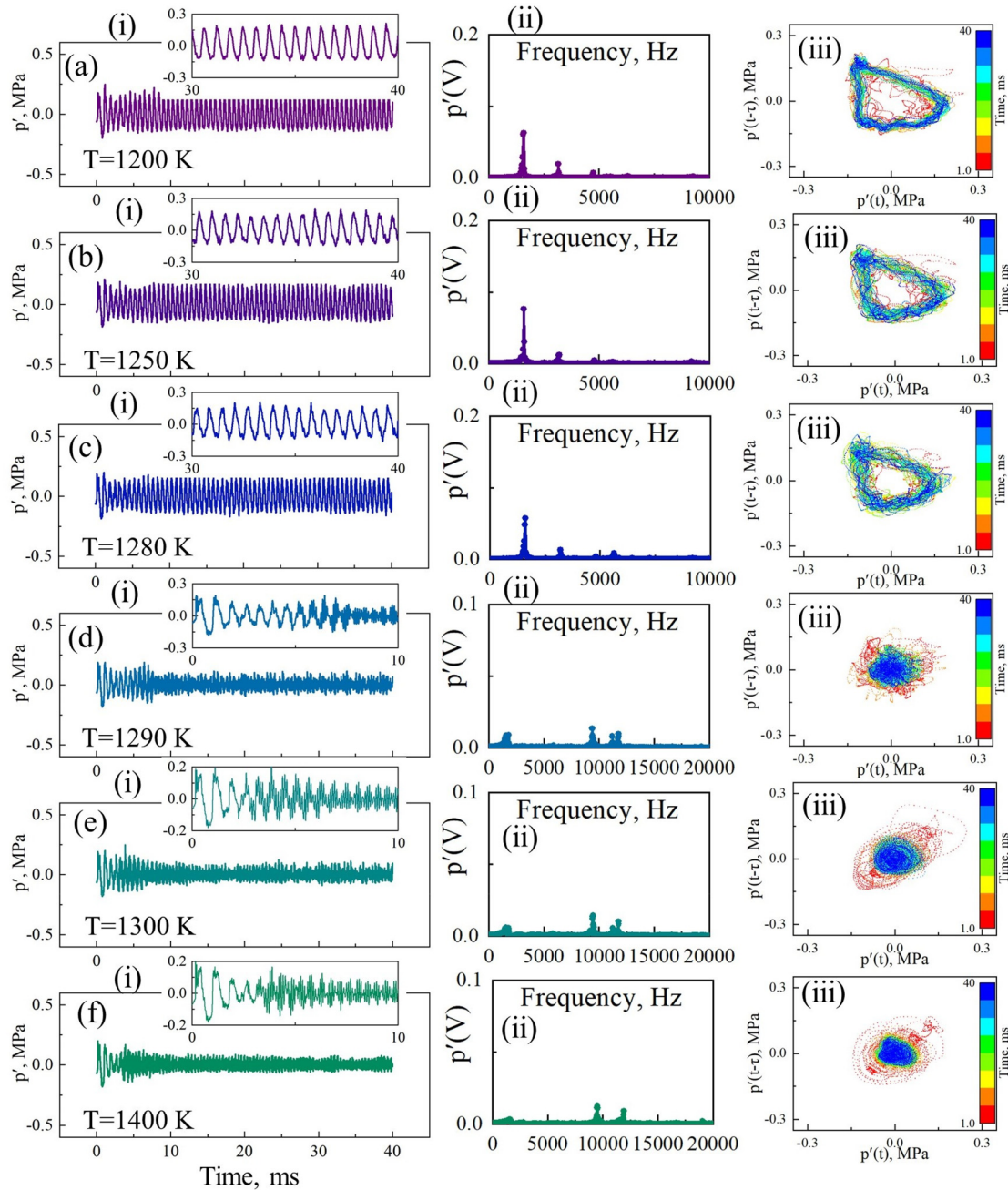


FIG. 11. Overview of the second bifurcation process of the system dynamics under the parameter space of oxidizer inlet temperature ($1200\text{ K} \leq T \leq 1400\text{ K}$): (a)–(f) The time series of pressure monitored at probe 1; (i) magnified local time series of pressure; (ii) normalized amplitude spectrum results ($p'(V) = p'/\bar{p}$); and (iii) the phase space trace of the pressure. The color bar shows the time evolution from 1 to 40 ms.

between 0 and 10 ms, followed by a subsequent transition to another oscillatory state characterized by temporal variations in frequency. Subsequent FFT results showed that the dominant frequencies of these two oscillations were 1820 and 9384 Hz, respectively. The first frequency is the first-order acoustic frequency (f_1) of the combustion

chamber, and the second dominant frequency (based on our previous discussion) can be identified as close to the intrinsic hydrodynamic instability frequency ($f \approx 10\text{ kHz}$). This is a new phenomenon that has not been previously reported in the published literature. In previous studies,^{26,36,43,62} it was generally believed that the pressure spectrum

characteristic of the combustion noise state was a wideband noise around the natural acoustic frequency (f_n), which was considered independent of intrinsic hydrodynamic instability. As the inlet temperature of the oxidizer continues to increase ($1300\text{ K} \leq T \leq 1400\text{ K}$), the duration of the acoustic oscillation with f_1 as the dominant frequency is further shortened. According to the FFT results, it can also be observed

that the pressure amplitude is suppressed near the natural acoustic frequency. The phase diagram results also show that the phase space trajectory of the state variable at this time is a circular region around the central point, and no obvious repetitive pattern is observed.

Figure 12(a) shows the instantaneous spatial distribution results of the spanwise vorticity in the y - z plane and the x - z plane when the

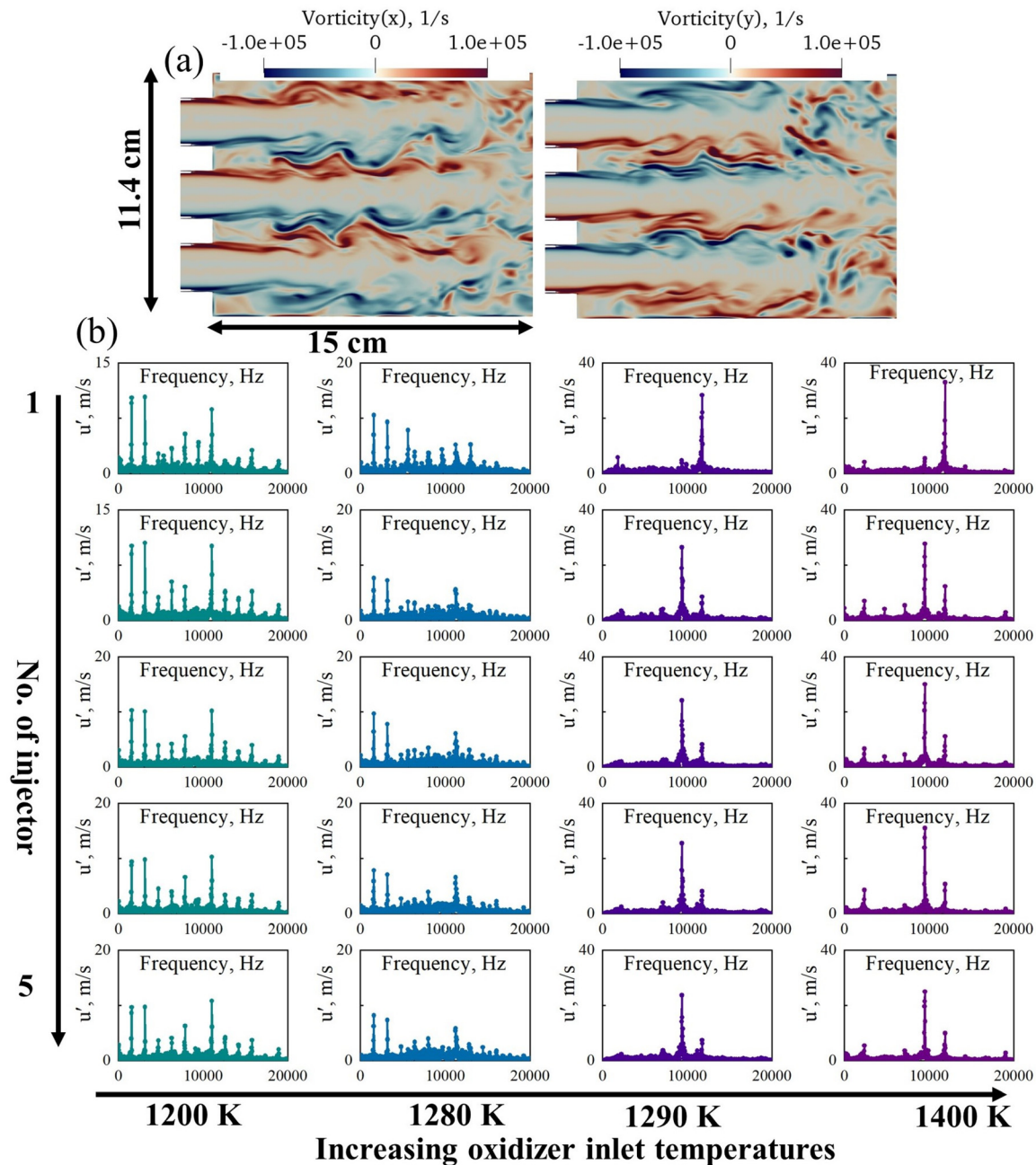


FIG. 12. (a) At $T = 1200\text{ K}$, the spatial distribution results of X-direction vorticity in the y - z plane and Y-direction vorticity in the x - z plane at an instantaneous snapshot. (b) The FFT results of radial velocity signals monitored at probes 2, 3, 4, 5, and 6. The oxidizer inlet temperatures ranged from left to right: 1200, 1280, 1290, and 1400 K. The injectors are numbered as follows from top to bottom: Injector No. 1 to Injector No. 5.

oxidizer inlet temperature is 1200 K. The findings demonstrate the formation of a larger-scale coherent structure downstream of the dump plane during thermoacoustic instability. In comparison to the combustion noise state of the pre-thermoacoustic instability regime, there was an enhanced coupling between Injector No. 1 and its surrounding injector elements. Downstream of Injector No. 1 and its surrounding injector element, the interaction of wake flow regions is observed, which has the potential to amplify or sustain thermoacoustic instability.

The FFT results of radial velocities monitored at probes 2, 3, 4, 5, and 6 during the second bifurcation ($1200\text{ K} \leq T \leq 1400\text{ K}$) are depicted in Fig. 12(b), which captures the time evolution of vortex dynamics for each Injector element (Injectors No. 1–5) near the initial shear layer. At $T = 1200\text{ K}$, the dominant spectral response of the five injector elements' radial velocities is observed at two acoustic frequencies ($f_1 = 1590\text{ Hz}$, $f_2 = 3154\text{ Hz}$) and intrinsic hydrodynamic instability frequencies ($f_{\text{vortex}} = 11\,050\text{ Hz}$). Notably, there are discernible variations in amplitudes corresponding to the same frequency; for instance, Injector No. 1 and Injector No. 2 exhibit predominance at frequency f_2 while Injector No. 3 demonstrates predominance at

frequency f_1 . On the other hand, Injector No. 4 and Injector No. 5 show dominance at frequency f_{vortex} . As we approach the boundary of the bifurcation region ($T = 1280\text{ K}$), it is evident that spectral response characteristics of radial velocities for all five jets are primarily dominated by frequency f_1 . With a slight increase in oxidizer temperature ($T = 1290\text{ K}$), a qualitative shift occurs in system dynamics leading to a second bifurcation phenomenon. In this case, radial velocity spectral response peaks near intrinsic hydrodynamic instability frequency while being suppressed near natural acoustic frequency. Regarding the frequencies associated with vortex shedding process, Injector No. 1 demonstrates dominance at a frequency of $11\,768\text{ Hz}$, while Injectors No. 2–5 exhibit a higher dominance frequency of 9384 Hz . Interestingly enough, both Injectors No. 2 and 5 display small peaks around $11\,768\text{ Hz}$ indicating that the vortex core downstream of Injector No. 1 also passes through this location thereby providing quantitative numerical evidence for injector–injector interaction within the combustion noise state after the thermoacoustic regime. The radial velocity responses remain consistent between $T = 1400\text{ K}$ and $T = 1290\text{ K}$ and is not repeated.

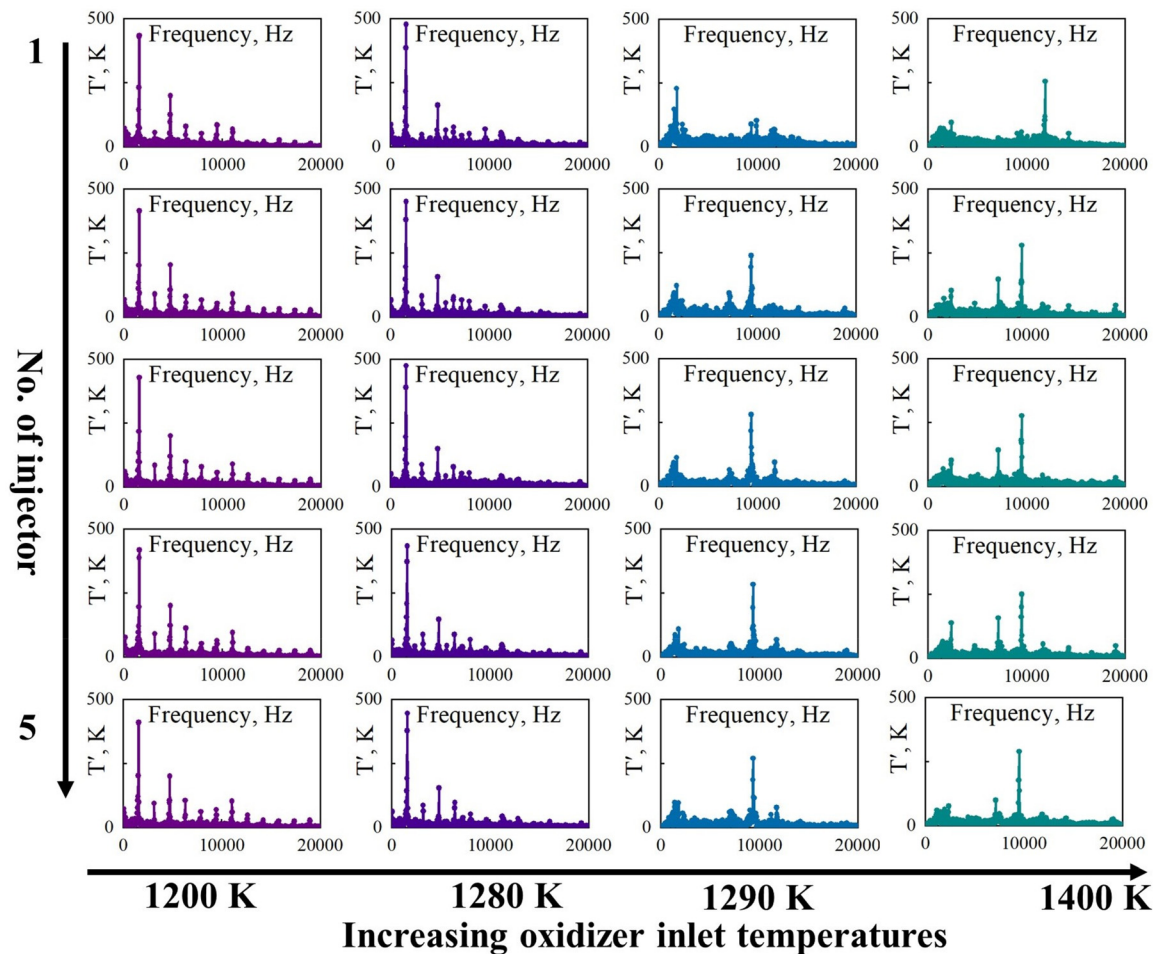


FIG. 13. The FFT results of temperature signals monitored at probes 2, 3, 4, 5, and 6. The oxidizer inlet temperatures ranged from left to right: 1200, 1280, 1290, and 1400 K. The injectors are numbered as follows from top to bottom: Injector No. 1 to Injector No. 5.

The spectral response of the temperature field at the initial shear layer downstream of each injector during the second bifurcation process ($1200\text{ K} \leq T \leq 1400\text{ K}$) is illustrated in Fig. 13. In this case, the frequency response of the temperature field exhibits similarity to that of the pressure disturbance. Within the range of $1200\text{ K} \leq T \leq 1280\text{ K}$, the temperature spectral response at the initial shear layer downstream of all five jets is primarily influenced by the first-order acoustic frequency (f_1), while being suppressed near the natural hydrodynamic frequency ($f_{\text{vortex}} \approx 10\text{ kHz}$). As the oxidizer inlet temperature ($T = 1290\text{ K}$) is further increased, Injector No. 1 exhibits a dominant spectrum response frequency for temperature at 1820 Hz , while Injectors No. 2–5 demonstrate a dominant spectrum response frequency for temperature at 9384 Hz . These findings contribute to our comprehensive understanding of the intricate coupling mechanism among injectors within multi-injector systems. When the oxidizer inlet temperature reaches its maximum value of 1400 K , both temperature and radial velocity oscillations for Injector No. 1 are locked at a frequency of $11\,922\text{ Hz}$, whereas Injectors No. 2–5 exhibit locked frequencies for their respective temperatures and radial velocities at approximately 9538 Hz . The disparity in responses between Injector No. 1 and Injectors No. 2–5 can be attributed to variations caused by nozzle effects downstream of the combustion chamber.

D. Spatiotemporal analysis of combustion flow fields during the transition to limit cycle state

This section focuses on the spatiotemporal evolution of the combustion flow field under different dynamical states using instantaneous snapshot analysis, vorticity transport, flame index analysis, and other techniques to elucidate the driving mechanism behind combustion instability in the multi-bifurcation process. Figure 14 illustrates an instantaneous snapshot of the combustion field during the first bifurcation. Notably, high-pressure waves are observed near the head of the combustion chamber for comparison purposes. At $T = 400\text{ K}$, a continuous distribution of methane and oxygen mass fractions is observed without distinct wrinkles. Simultaneously, this case exhibits the lowest combustion temperature with minimal interference between flow regions downstream of each injector. Upon increasing the oxidizer inlet temperature ($T = 500\text{ K}$), a small vortex structure emerges at the fuel-oxygen interface. As oxidizer inlet temperature further increases ($T = 600\text{ K}$, $T = 800\text{ K}$), a limit cycle state is reached where interruption occurs in fuel flow from injectors upon entering the combustion chamber due to high-pressure wave effects near the dump plane. Downstream of the dump plane, coherent structures appear in unburned reaction flow and temperature fields with significantly elevated combustion temperatures. Importantly, in the wake of Injector No. 1, methane mass fraction

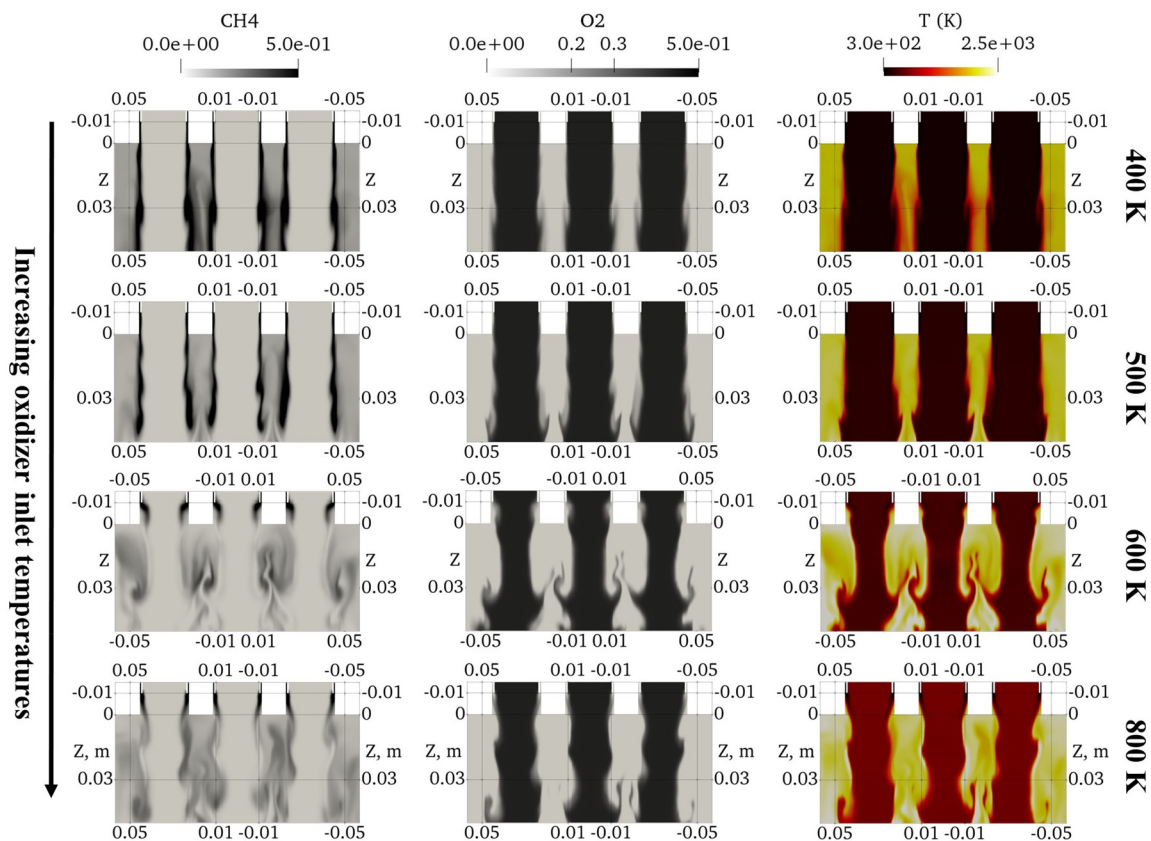


FIG. 14. Instantaneous spatial distribution results of methane mass fraction (left), oxygen mass fraction (middle) and temperature (right) at different oxidizer inlet temperatures during the first bifurcation process. The instantaneous moment corresponding to the snapshot is when a high-pressure wave occurs near the dump plane.

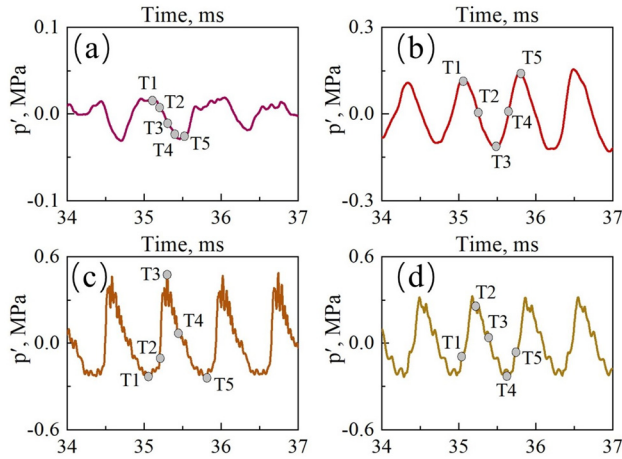


FIG. 15. Time series of pressure monitored at probe 1 under different oxidizer inlet temperature: (a) $T = 400$, (b) $T = 500$, (c) $T = 600$, and (d) $T = 800$ K. The marked circles represent five moments of interest within the acoustic oscillation cycle.

notably interferes with that of Injector No. 2 and Injector No. 3 near $z = 3$ cm, providing detailed evidence for coupling between injectors during thermoacoustic instability.

The periodic snapshot analysis offers more detailed insights into the vortex evolution process under different dynamical states. Hence, Fig. 15 illustrates the time series of local pressure monitored at probe 1 during the initial bifurcation process, wherein five noteworthy moments are identified as the foundation for subsequent analysis. Figure 16 shows spanwise vorticity snapshots and streamlines at various time moments throughout the first bifurcation process. At $T = 400$ K, the combustion chamber exhibits solely low-amplitude and aperiodic acoustic oscillations, while the temporal evolution of the combustion flow field is primarily governed by intrinsic hydrodynamic instability rather than acoustic oscillations. Consequently, this operating condition exclusively focuses on elucidating the spatiotemporal evolution process of the combustion flow field at a small time increment, with an aim to unveil the high-frequency vortex shedding phenomenon ($f = 4230$ Hz). For $T = 400$ K, near the dump plane, we observe a display of minimal vorticity magnitude owing to the oxidizer inlet temperature being in proximity to that of methane, resulting in a

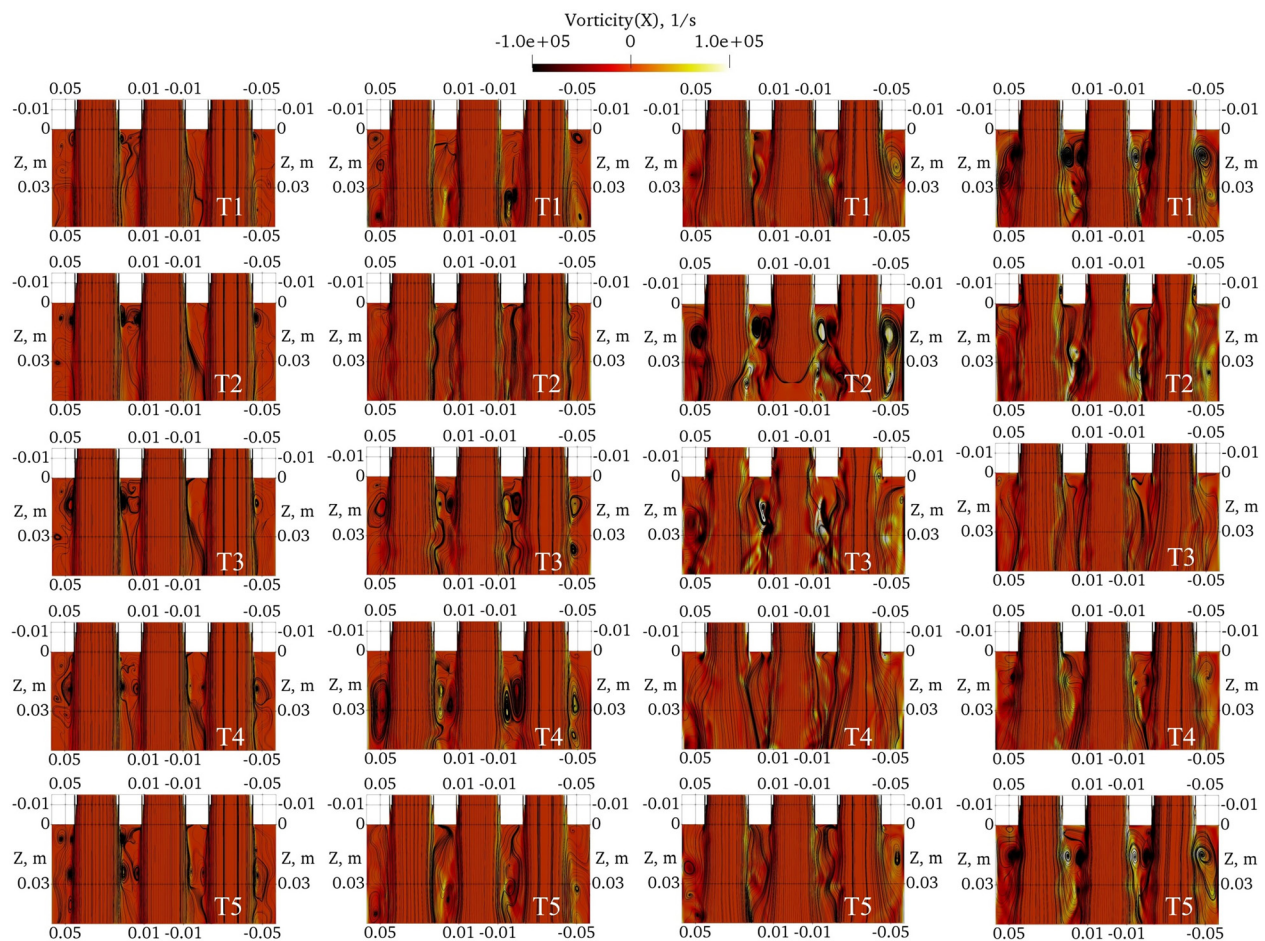


FIG. 16. The snapshots of spanwise vorticity at varying time moments under different oxidizer inlet temperatures. The streamline is represented by the black line. Left to right: $T = 400, 500, 600$, and 800 K. Top to bottom: five specific moments of interest.

reduced density ratio between oxidizer and fuel. Simultaneously, due to insufficient pressure oscillation amplitude within the combustion chamber, large-scale coherent structures near the shear layer fail to form; instead, continuous small vortex structures are observed. Moreover, there is less overlap among streamlines downstream of Injector No. 2 (left side of cross section), Injector No. 3 (right side of cross section), and Injector No. 1 (central cross section), indicating weaker coupling strength between injectors. With an appropriate increase in the oxidizer inlet temperature ($T = 500$ K), a periodic pressure oscillation with moderate amplitude emerges within the combustion chamber, as depicted in Fig. 15. At T1, the pressure wave propagates around $z = 1$ cm, accompanied by the appearance of several small vortices within the recirculation area. Notably, between the wakes of Injector No. 1 and Injector No. 3 (near $z = 3$ cm) in the recirculation region, a vortex structure formed by two sets of overlapping streamlines is observed. At T3, when the high-pressure wave moves away from the dump plane vicinity, six vortex structures are observed within the recirculation region

ranging from $0 \text{ cm} \leq z \leq 3 \text{ cm}$. These vortices are situated between Injector No. 2 and the combustion chamber wall, between the wakes of Injector No. 2 and Injector No. 1, as well as between the wakes of Injector No. 1 and Injector No. 3, along with an area between Injector No. 1 and the combustion chamber wall. Over time (at moment T4), these vortices gradually convect downward while enlarging to form a larger vortex structure near $z = 3$ cm. Eventually, after reaching near the initial shear layer at time T5, these vortices were completely shed due to interaction with high-pressure waves. As we increase oxidizer inlet temperature further into $T = 600$ K at moment T3 or even up to $T = 800$ K at moment T2 similar phenomena occur where internal vortex formation is observed inside the respective injectors. In addition, it is noteworthy that increasing oxidizer inlet temperature leads to an elevated density ratio of fuel to oxidizer resulting in enhanced progressive vorticity near the initial shear layer.

In the following, we shall present the flame index analysis as a tool for discerning between diffusion flames and premixed flames in

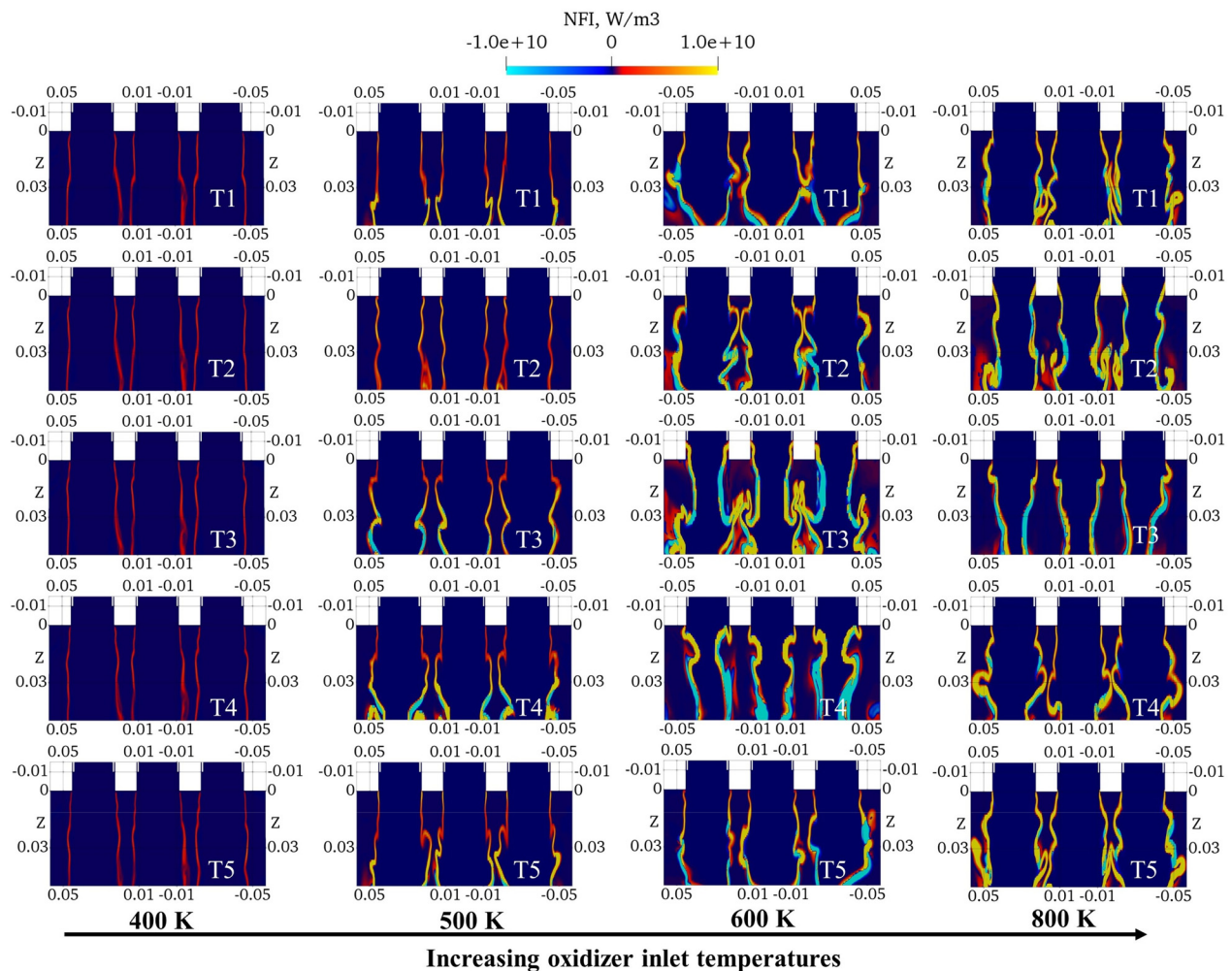


FIG. 17. The snapshots of the flame index at varying time moments under different inlet temperatures of the oxidizer. The streamline is represented by the black line. Left to right: $T = 400, 500, 600$, and 800 K. Top to bottom: five specific moments of interest.

multi-element rocket combustors. The mathematical formulation for the flame index⁶³ is as follows:

$$FI = \frac{\nabla Y_F \cdot \nabla Y_O}{|\nabla Y_F \cdot \nabla Y_O|}. \quad (7)$$

The local mass fraction of methane is represented by Y_F , while the mass fraction of oxygen is denoted as Y_O . The given equation only allows for values of +1, -1, or 0 exclusively. Specifically, a value of +1 corresponds to premixed flames, whereas non-premixed flames are associated with a value of -1 and no-flame conditions result in a value of 0. In this paper, following Nguyen and Sirignano,²⁵ the flame index was combined with the heat release rate to prevent the occurrence of pseudo-flame structures. The mathematical expression is as follows:

$$NFI = FI \cdot HRR, \quad (8)$$

where HRR represents the heat release rate (W/m^3).

The instantaneous spatial distribution results of the flame index (NFI) during the first bifurcation are presented in Fig. 17, with time moments of interest matching those in Fig. 15. It is evident from the figure that variations in the inlet temperature of the oxidizer significantly impact flame dynamics. First, there are notable differences in the spatial distribution of flame heat release. At lower oxidant inlet temperatures, minimal heat release distribution near the dump plane is observed. However, as the inlet temperature increases, a clear rise in heat release becomes apparent. Second, distinct variations can be seen in combustion mode characteristics. At lower oxidant inlet temperatures, premixed flames ($NFI > 0$, red) dominate. As the inlet temperature rises, diffusion flames ($NFI < 0$, blue) start to appear within the flame region. For $T = 400$ K, a continuously distributed flame surface without prominent wrinkles indicates that premixed flames prevail as dominant combustion modes. Specifically, at $T = 500$ K and moments T1 and T5, high-pressure waves propagate near the dump plane, whereas at moment T3, they move away from the head position of the combustion chamber. Moderate amplitude pressure oscillation leads to wrinkling of the flame surface and noticeable forward movement of heat release positions occurs at this stage for $T = 500$ K conditions. Enhanced interference between flames is observed as downstream heat release areas from different injectors begin to converge closer together due to these effects on combustion dynamics. At moments T3 and T4 specifically, diffusion flames start appearing ($3 \text{ cm} \leq z \leq 5 \text{ cm}$). When thermoacoustic instability occurs ($T = 600$ K), the flame surface exhibits significant distortion. At T3, the pressure wave propagates near the dump plane. Two noteworthy changes in flame dynamics are observed: (1) Substantial combustion also takes place within the injector. (2) The downstream flame area of Injector No. 1 starts to overlap with that of Injectors No. 2 and 3, indicating a strong coupling relationship between injectors. A similar phenomenon is observed at $T = 800$ K (T2).

Figure 18(a) shows the time-averaged distribution of the total flame heat release along the engine axis. The time range is set at 35–50 ms, with a sampling interval of 0.05 ms. For the total heat release, the mathematical expression is

$$HRR = \int_z^{z+2cm} \left(\iint QdS \right) dz, \quad (9)$$

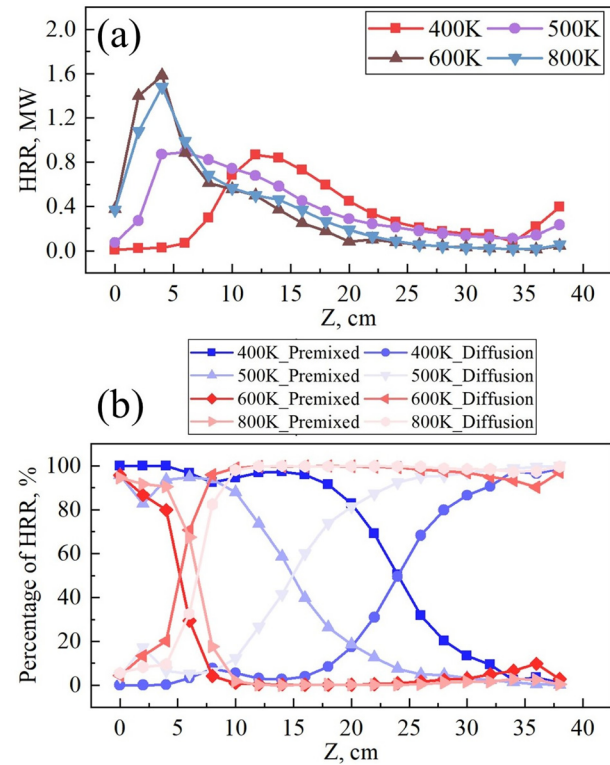


FIG. 18. The time-averaged results of the combustion field during the first bifurcation process: (a) the total amount of flame heat release and (b) the spatial distribution of the total amount of heat release corresponding to different combustion modes along the z-axis.

where Q represents the heat release per unit volume (W/m^3), S represents the cross-sectional area, and the value of the axial coordinate z is $z = -1, 1, 3, 5, 7, 9, \dots, 35, 37 \text{ cm}$. Therefore, HRR (W) represents the total heat release of the combustion chamber portion at a height of 2 cm. As depicted in the figure, at an oxidizer inlet temperature of 400 K, there is a significant downward shift of the heat release region, reaching its maximum value within the range of $11 \text{ cm} \leq z \leq 13 \text{ cm}$. Simultaneously, no discernible combustion phenomenon is observed near the top of the combustion chamber. When the oxidizer inlet temperature increases to 500 K, the flame exhibits its maximum heat release between $5 \text{ cm} \leq z \leq 7 \text{ cm}$; however, only a minor amount of combustion persists within $-1 \text{ cm} \leq z \leq 1 \text{ cm}$. Interestingly, under thermoacoustic instability conditions ($T = 600$ and $T = 800$ K), similar to previous cases, peak heat release occurs within the range of $3 \text{ cm} \leq z \leq 5 \text{ cm}$ with nearly identical total heat release in $-1 \text{ cm} \leq z \leq 1 \text{ cm}$. More specifically, at $T = 600$ K, the maximum heat release ($5 \text{ cm} \leq z \leq 7 \text{ cm}$) surpasses that observed at $T = 800$ K. This discrepancy can be attributed to the significantly higher amplitude of acoustic oscillations at $T = 600$ K compared to $T = 800$ K, as depicted in Fig. 8. The increased amplitude of acoustic oscillations leads to a more concentrated and localized distribution of heat release near the dump plane.

The distribution of the total heat release corresponding to different combustion modes after screening with the flame index sign (plus

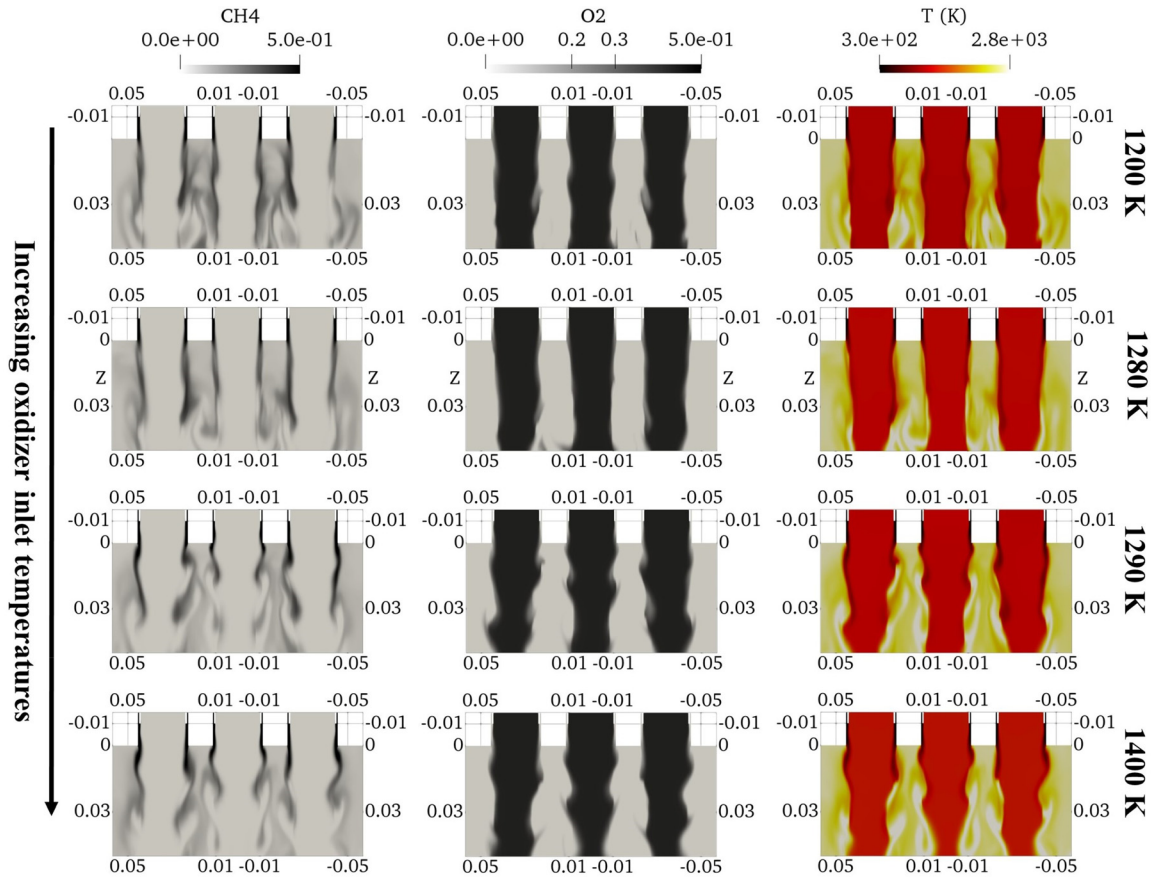


FIG. 19. Instantaneous spatial distribution results of methane mass fraction (left), oxygen mass fraction (middle), and temperature (right) at different oxidizer inlet temperatures during the second bifurcation process. The instantaneous moment corresponding to the snapshot is when a high-pressure wave occurs near the dump plane.

or minus) along the engine axis is presented in Fig. 18(b). The mathematical form of the percentage of HRR after screening is defined based on the sign of flame index, as follows:

$$\begin{cases} \text{Percentage of HRR}|_{NFI>0} = \frac{HRR|_{NFI>0}}{HRR}, \\ \text{Percentage of HRR}|_{NFI<0} = \frac{HRR|_{NFI<0}}{HRR}. \end{cases} \quad (10)$$

At $T = 400$ K, the premixed flame is predominantly located at the front end of the combustion chamber. As unburned reactants convect downward, diffusion flames start to emerge. In the region of $23 \text{ cm} \leq z \leq 25 \text{ cm}$, there is an almost equal proportion of premixed and diffusion flames. Further convection leads to diffusion flames dominating in the second half of the combustion chamber. These qualitative trends are nearly identical, with some differences observed: (1) with increasing oxidizer inlet temperature, the position of the equilibrium ratio (50%) of the diffusion flame and the premixed flame moves toward the front of the combustion chamber. (2) In the thermoacoustic instability regime ($T = 600$ K, $T = 800$ K), the position of the equilibrium ratio at $T = 600$ K ($6 \text{ cm} \leq z \leq 7 \text{ cm}$) is closer to the dump

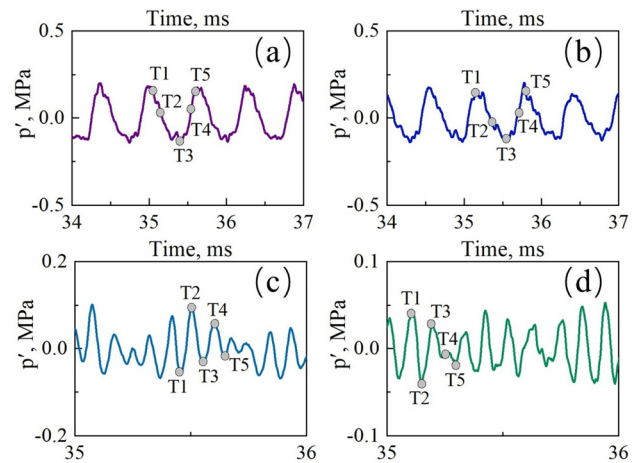


FIG. 20. Time series of pressure monitored at probe 1 under different oxidizer inlet temperatures: (a) $T = 1200$, (b) $T = 1280$, (c) $T = 1290$, and (d) $T = 1400$ K. The marked circles represent five moments of interest within the acoustic oscillation cycle.

plane compared to the equilibrium position at $T = 800$ K ($7 \text{ cm} \leq z \leq 9 \text{ cm}$). This discrepancy arises due to larger pressure oscillation amplitude when $T = 600$ K. Both pressure oscillation and oxidizer inlet temperature significantly influence the spatial distribution of combustion modes.

E. Spatiotemporal analysis of combustion flow dynamics during secondary Hopf bifurcations

The instantaneous spatial distribution of methane mass fraction, oxygen mass fraction, and temperature field during the second bifurcation process is illustrated in Fig. 19. The selected moment corresponds to the high-pressure wave near the dump plane. Within the temperature range of $1200 \text{ K} \leq T \leq 1280 \text{ K}$, the thermoacoustic system remains in a period-1 limit cycle state. During this phase, it can be observed that the fuel (methane) jet is continuously distributed near the dump plane due to a significant reduction in pressure oscillation amplitude within the combustion chamber, resembling a state of combustion

noise. Approximately 3 cm downstream from the dump plane, interference between methane wakes from different injectors indicates moderate-intensity coupling among them. For temperatures ranging from $1290 \text{ K} \leq T \leq 1400 \text{ K}$, we observe that even without or with weak acoustic oscillations present, intrinsic hydrodynamic instability still leads to typical spatial distribution patterns of jet flow. Additionally, owing to a high-density ratio between fuel and oxidizer, wrinkles are also observed in unburnt oxygen and fuel jets near the dump plane. Simultaneously, due to elevated oxidizer inlet temperatures at this stage, substantial heat release occurs close to the dump plane—a phenomenon distinct from conditions before the thermoacoustic instability regime.

Figure 20 displays the time series of local pressure monitored at probe 1 during the second bifurcation process, with five significant moments marked as the basis for subsequent snapshot analysis. Figure 21 presents spanwise vorticity snapshots and streamlines of four conditions at different times during the second bifurcation process. Compared to $T = 600$ and $T = 800$ K, no vortex structure inside the

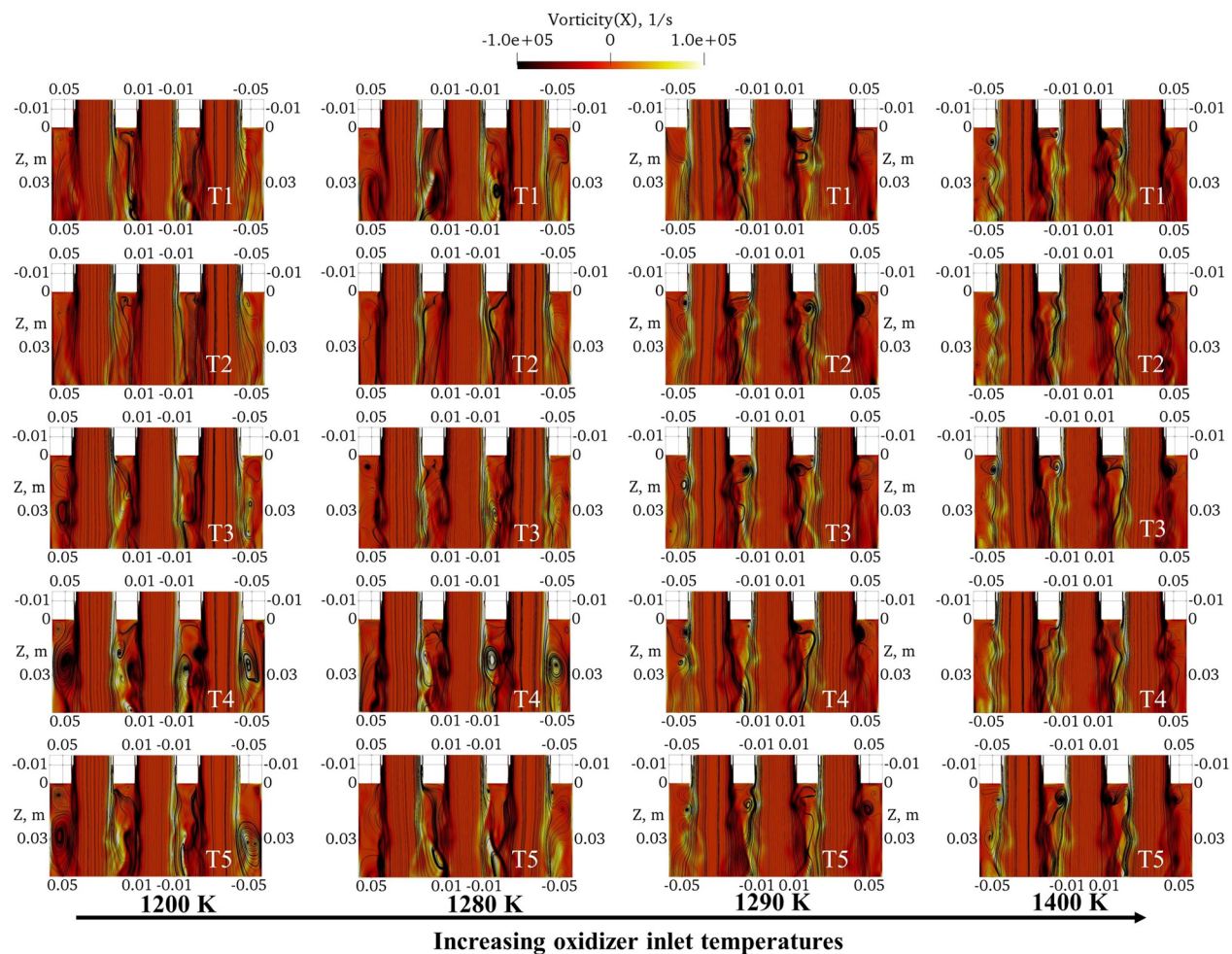


FIG. 21. The snapshots of spanwise vorticity at varying time moments under different inlet temperatures of the oxidizer. The streamline is represented by the black line. Left to right: $T = 1200, 1280, 1290$, and 1400 K. Top to bottom: Five specific moments of interest.

injector is observed due to small amplitude pressure disturbance when high-pressure waves pass near the initial shear layer (time T1 and time T5) at $T = 1200$ K. During $T1 \rightarrow T2$, pressure waves propagate downstream from the initial shear layer to the combustion chamber; however, because vortex dynamics processes were completed in previous acoustic oscillation periods at T1, no large-scale vortex structures were observed in recirculation areas. During $T4 \rightarrow T5$, high-pressure waves travel downstream from combustion chambers toward the vicinity of initial shear layers reaching this position at T5; coherent structures appear in recirculation regions with multiple vortex structures of varying geometric sizes near shear layers that may explain multiple dominant peaks in FFT results for radial velocity. When temperatures are set at either 1290 or 1400 K, pressure oscillation amplitudes are too small to dominate spatiotemporal dynamics within combustion flow fields; instead, intrinsic hydrodynamic instability plays a dominant role. Compared to the thermoacoustic instability conditions above, there exists only a small-scale vortex structure but no coherent

structure within lower reaches of the dump plane; however, compared to previous combustion noise, there is a significant increase in magnitude for spanwise vorticity within the shear layer region which can be attributed to density ratio changes between oxidizer and fuel.

The spatiotemporal distribution of the flame index (NFI) at different oxidant inlet temperatures during the second bifurcation is depicted in Fig. 22. In comparison with the results obtained from the first bifurcation process, several noteworthy distinctions can be observed: (a) All four operating conditions exhibit anchored flames within the recirculation zone, devoid of any combustion occurrence in the upstream region of the dump plane. The precise positioning of flame roots at the dump plane ($z=0$) indicates premixed flames. (b) The downstream flame regions in the wake of different injectors demonstrate enhanced independence from one another, indicating weaker coupling strength between injectors. (c) Particularly, significant advancements of flame heat release region toward dump plane within the range of $1290 \text{ K} \leq T \leq 1400 \text{ K}$ are observed when compared to

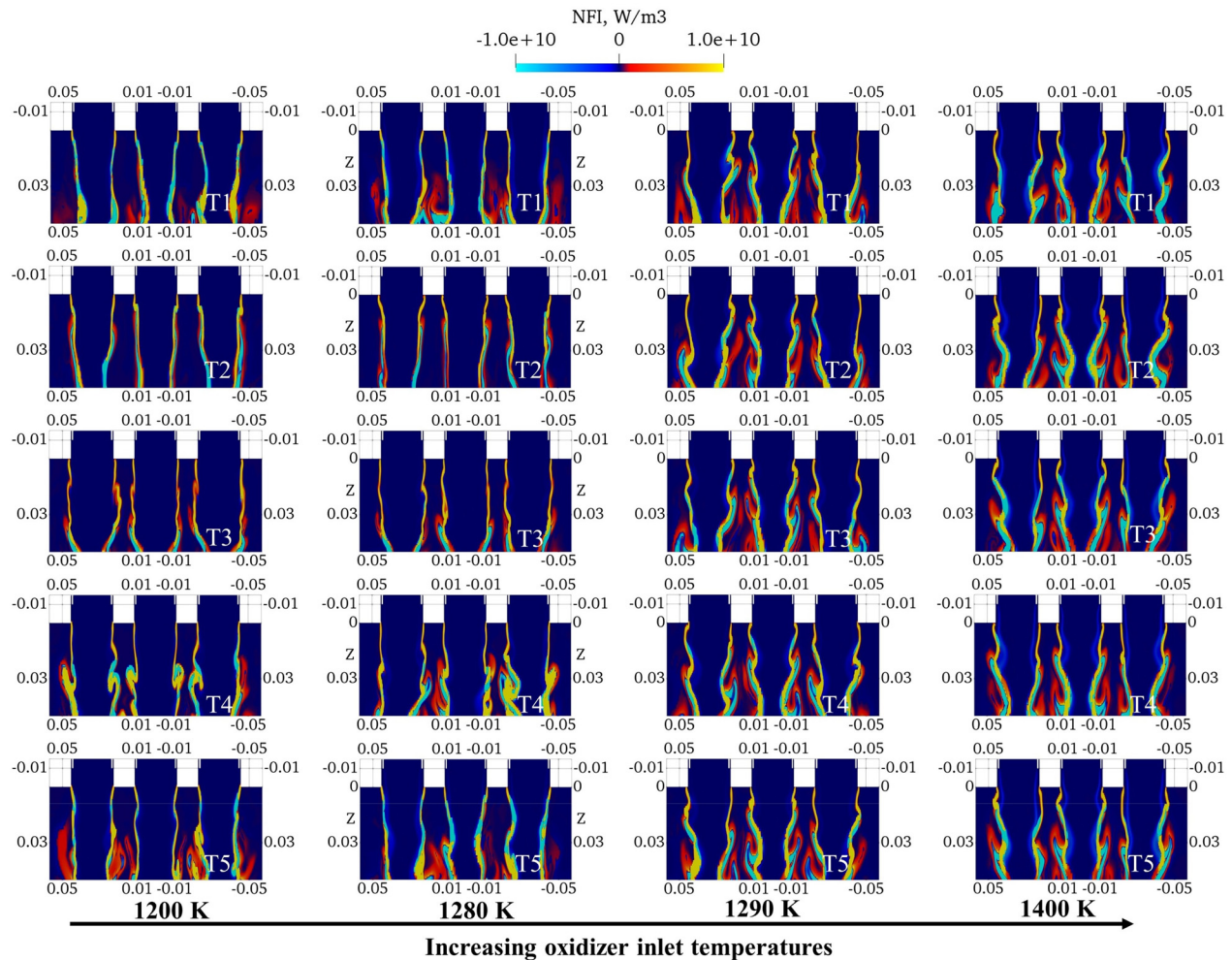


FIG. 22. The snapshots of the flame index at varying time moments under different inlet temperatures of the oxidizer. The streamline is represented by the black line. Left to right: $T = 1200, 1280, 1290$, and 1400 K. Top to bottom: Five specific moments of interest.

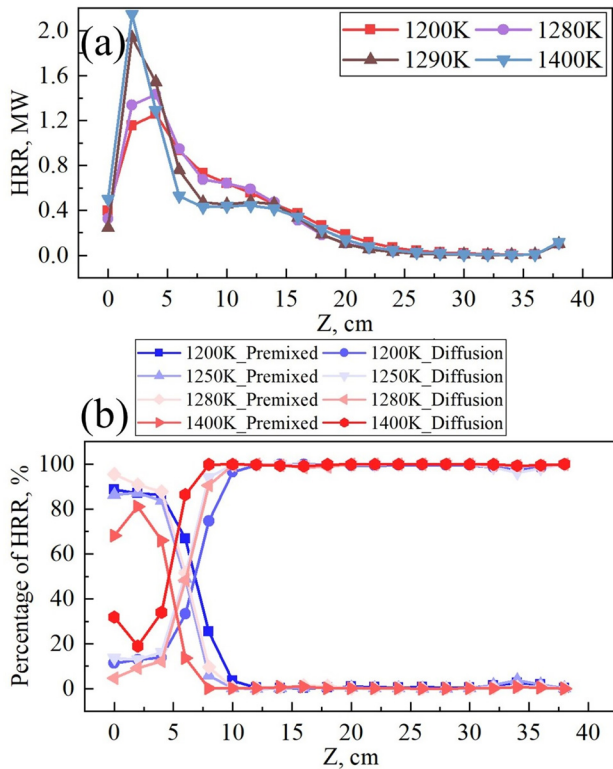


FIG. 23. The time average results of the combustion field in the second bifurcation process: (a) the total amount of flame heat release and (b) the spatial distribution of the total amount of heat release corresponding to different combustion modes along the z-axis.

states of combustion noise before thermoacoustic instability regimes. Additionally, there is a substantial increase in diffusion flame proportion.

As a quantitative comparison of the spatial distribution heat release and corresponding combustion modes, Fig. 23 compares the time-averaged flame heat release during the second bifurcation process and the corresponding different combustion modes with the axial position of the engine. An interesting phenomenon is that the maximum heat release position corresponding to the combustion noise state after the thermoacoustic instability regime is closer to the dump plane than the maximum heat release position in the thermoacoustic instability regime. The results of figure (b) further reveal that the premixed flame always dominates the combustion mode in the front of the combustion chamber, while the diffusion flame dominates the combustion mode at the end of the combustion chamber. The position of the equilibrium ratio (50%) of the diffusion flame and the premixed flame moves upstream with the increase in oxidizer inlet temperature. The position of the equilibrium ratio of the combustion noise state after the thermoacoustic instability regime is closer to the upstream of the dump plane than that of before the thermoacoustic instability regime.

IV. CONCLUSIONS

In this paper, the longitudinal thermoacoustic instability in a multi-element model rocket combustor burning hydrogen peroxide and methane is investigated based on the detached eddy simulation

method. First, the numerical framework of this paper is verified based on a single-element model rocket combustor burning hydrogen peroxide/methane. After achieving grid independence, in the parameter space of the inlet temperature of the oxidizer, we mainly focus on (i) the multi-bifurcation process before and after the thermoacoustic instability regime; (ii) the frequency-locking relationship in the wake of different injectors under different dynamical states; and (iii) spatio-temporal evolution of combustion flow fields during the multi-bifurcation process. Our conclusions are as follows:

- (1) In the parameter space of oxidizer inlet temperature, the system dynamics undergo two bifurcation processes. During the first bifurcation, when $400\text{ K} \leq T \leq 800\text{ K}$, the system dynamics enter a complete period-1 limit cycle state ($600\text{ K} \leq T \leq 800\text{ K}$) through intermittent oscillation ($400\text{ K} \leq T \leq 500\text{ K}$). As the oxidizer inlet temperature continues to increase ($1200\text{ K} \leq T \leq 1400\text{ K}$), a second bifurcation occurs resulting in a direct transition of the system dynamics from a medium amplitude period-1 limit cycle state ($1200\text{ K} \leq T \leq 1280\text{ K}$) back to combustion noise state ($1290\text{ K} \leq T \leq 1400\text{ K}$).
- (2) The analysis of vortex shedding frequency in the wakes of various injectors reveals the intricate coupling mechanism between them. In intermittent oscillation conditions prior to reaching the thermoacoustic instability regime, the downstream vortex shedding process is governed by a competitive and cooperative relationship between the natural acoustic mode (f_n) and intrinsic hydrodynamic mode (f_{vortex}). However, even under identical dynamical states (or operating conditions), there may still be variations in the dominant frequency of vortex shedding in the wakes of different injectors. Meanwhile, during combustion noise state, only small downstream vortex structures are observed within that region, indicating weak coupling strength between injectors. In a strong thermoacoustic instability regime, vortices from different injectors interfere with each other signifying strong coupling strength between them.
- (3) When the oxidizer inlet temperature ranges from 400 to 1280 K, the temperature spectrum at the initial shear layer downstream of each injector exhibits a distribution characteristic similar to that of the pressure spectrum, indicating dominance of first-order acoustic frequency. As the oxidizer inlet temperature increases, both temperature oscillations and vortex dynamics reach a frequency-locked state at intrinsic hydrodynamic modes rather than acoustic modes. The increase in oxidizer inlet temperature causes displacement of the flame anchor point and main heat release area toward the dump plane. Both pressure oscillation and oxidizer inlet temperature significantly affect spatial distribution characteristics of combustion modes. Premixed flames primarily occur at the front section while diffusion flames appear toward the end section of the combustion chamber. The equilibrium position for diffusion flame and premixed flame (each accounting for 50% total heat release) shifts toward the dump plane with increasing oxidizer inlet temperature and pressure oscillation amplitude.

ACKNOWLEDGMENTS

This work was supported by the Fund-supported Project: the Key Project of National Natural Science Foundation of China (U2241250).

AUTHOR DECLARATIONS

Conflict of Interest

The authors have no conflicts to disclose.

Author Contributions

Yuanzhe Liu: Conceptualization (lead); Data curation (lead); Formal analysis (lead); Investigation (lead); Methodology (lead); Software (lead); Validation (lead); Visualization (lead); Writing – original draft (lead). **Zhuopu Wang:** Conceptualization (equal); Project administration (lead); Supervision (lead); Writing – review & editing (equal). **Wen Ao:** Writing – review & editing (equal). **Yu Guan:** Supervision (lead); Writing – review & editing (lead). **Peijin Liu:** Conceptualization (equal); Funding acquisition (lead); Supervision (equal); Writing – review & editing (equal).

DATA AVAILABILITY

The data that support the findings of this research are available from the corresponding author upon reasonable request.

REFERENCES

- ¹T. Poinot, “Prediction and control of combustion instabilities in real engines,” *Proc. Combust. Inst.* **36**(1), 1–28 (2017).
- ²M. P. Juniper and R. I. Sujith, “Sensitivity and nonlinearity of thermoacoustic oscillations,” *Annu. Rev. Fluid Mech.* **50**, 661–689 (2018).
- ³W. A. Sirignano, “Driving mechanisms for combustion instability,” *Combust. Sci. Technol.* **187**(1–2), 162–205 (2015).
- ⁴J. O’Connor, V. Acharya, and T. Lieuwen, “Transverse combustion instabilities: Acoustic, fluid mechanic, and flame processes,” *Prog. Energy Combust. Sci.* **49**, 1–39 (2015).
- ⁵J. C. Oefelin and V. Yang, “Comprehensive review of liquid-propellant combustion instabilities in F-1 engines,” *J. Propul. Power* **9**(5), 657–677 (1993).
- ⁶R. I. Sujith, M. P. Juniper, and P. J. Schmid, “Non-normality and nonlinearity in thermoacoustic instabilities,” *Int. J. Spray Combust. Dyn.* **8**(2), 119–146 (2016).
- ⁷P. P. Popov, A. Sideris, and W. A. Sirignano, “Stochastic modelling of transverse wave instability in a liquid-propellant rocket engine,” *J. Fluid Mech.* **745**, 62–91 (2014).
- ⁸V. K. Rani and S. L. Rani, “Development of a comprehensive flame transfer function and its application to predict combustion instabilities in a dump combustor,” *Combust. Sci. Technol.* **190**(8), 1313–1353 (2018).
- ⁹Y. Yu, S. Koeglmeier, J. Sisco, and W. Anderson, “Combustion instability of gaseous fuels in a continuously variable resonance chamber (CVRC),” AIAA Paper No. AIAA 2008-4657, 2008.
- ¹⁰A. S. Morgans and I. Duran, “Entropy noise: A review of theory, progress and challenges,” *Int. J. Spray Combust. Dyn.* **8**(4), 285–298 (2016).
- ¹¹G. M. R. Tamanampudi, S. Sardeshmukh, W. Anderson, and C. Huang, “Combustion instability modeling using multi-mode flame transfer functions and a nonlinear Euler solver,” *Int. J. Spray Combust. Dyn.* **12**(1), 175682772095032 (2020).
- ¹²M. Bauerheim, F. Nicoud, and T. Poinot, “Progress in analytical methods to predict and control azimuthal combustion instability modes in annular chambers,” *Phys. Fluids* **28**(2), 021303 (2016).
- ¹³T. Schuller, T. Poinot, and S. Candel, “Dynamics and control of premixed combustion systems based on flame transfer and describing functions,” *J. Fluid Mech.* **894**, P1 (2020).
- ¹⁴E. Lo Schiavo, D. Laera, E. Riber, L. Gicquel, and T. Poinot, “Effects of liquid fuel/wall interaction on thermoacoustic instabilities in swirling spray flames,” *Combust. Flame* **219**, 86–101 (2020).
- ¹⁵S. Gröning, J. S. Hardi, D. Suslov, and M. Oswald, “Injector-driven combustion instabilities in a hydrogen/oxygen rocket combustor,” *J. Propul. Power* **32**(3), 560–573 (2016).
- ¹⁶B. Pomeroy and W. Anderson, “Transverse instability studies in a subscale chamber,” *J. Propul. Power* **32**(4), 939–947 (2016).
- ¹⁷Y. C. Yu, J. C. Sisco, S. Rosen, A. Madhav, and W. E. Anderson, “Spontaneous longitudinal combustion instability in a continuously-variable resonance combustor,” *J. Propul. Power* **28**(5), 876–887 (2012).
- ¹⁸J. C. Sisco, Y. C. Yu, V. Sankaran, and W. E. Anderson, “Examination of mode shapes in an unstable model combustor,” *J. Sound Vib.* **330**(1), 61–74 (2011).
- ¹⁹E. L. Schiavo, D. Laera, E. Riber, L. Gicquel, and T. Poinot, “On the impact of fuel injection angle in Euler-Lagrange large eddy simulations of swirling spray flames exhibiting thermoacoustic instabilities,” *Combust. Flame* **227**, 359–370 (2021).
- ²⁰P. W. Agostinelli, D. Laera, I. Chterev, I. Boxx, L. Gicquel, and T. Poinot, “Large eddy simulations of mean pressure and H₂ addition effects on the stabilization and dynamics of a partially-premixed swirled-stabilized methane flame,” *Combust. Flame* **249**, 112592 (2023).
- ²¹A. Urbano, L. Selle, G. Staffelbach, B. Cuenot, T. Schmitt, S. Ducruix, and S. Candel, “Exploration of combustion instability triggering using Large Eddy Simulation of a multiple injector liquid rocket engine,” *Combust. Flame* **169**, 129–140 (2016).
- ²²K. Guo, Y. Ren, Y. Tong, W. Lin, and W. Nie, “Analysis of self-excited transverse combustion instability in a rectangular model rocket combustor,” *Phys. Fluids* **34**(4), 047104 (2022).
- ²³R. Garby, L. Selle, and T. Poinot, “Large-Eddy Simulation of combustion instabilities in a variable-length combustor,” *C. R. Méc.* **341**(1–2), 220–229 (2013).
- ²⁴M. E. Harvazinski, C. Huang, V. Sankaran, T. W. Feldman, W. E. Anderson, C. L. Merkle, and D. G. Talley, “Coupling between hydrodynamics, acoustics, and heat release in a self-excited unstable combustor,” *Phys. Fluids* **27**(4), 045102 (2015).
- ²⁵T. M. Nguyen and W. A. Sirignano, “The impacts of three flamelet burning regimes in nonlinear combustion dynamics,” *Combust. Flame* **195**, 170–182 (2018).
- ²⁶R. I. Sujith and V. R. Unni, “Complex system approach to investigate and mitigate thermoacoustic instability in turbulent combustors,” *Phys. Fluids* **32**(6), 061401 (2020).
- ²⁷K. Manoj, S. A. Pawar, J. Kurths, and R. I. Sujith, “Rijke tube: A nonlinear oscillator,” *Chaos* **32**(7), 072101 (2022).
- ²⁸L. Kabiraj and R. I. Sujith, “Nonlinear self-excited thermoacoustic oscillations: Intermittency and flame blowout,” *J. Fluid Mech.* **713**, 376–397 (2012).
- ²⁹Y. Liu, P. Liu, Z. Wang, W. Ao, and Y. Guan, “Large eddy simulation of combustion instability in a subcritical hydrogen peroxide/kerosene liquid rocket engine: Intermittency route to period-2 thermoacoustic instability,” *Phys. Fluids* **35**(6), 065145 (2023).
- ³⁰Y. Liu, P. Liu, Z. Wang, W. Ao, and Y. Guan, “Large eddy simulation of effects of oxidizer inlet temperatures on the transition routes before and after thermoacoustic instability in a subcritical hydrogen peroxide/kerosene liquid rocket engine,” *Phys. Fluids* **35**(12), 125141 (2023).
- ³¹Y. Guan, P. Liu, B. Jin, V. Gupta, and L. K. B. Li, “Nonlinear time-series analysis of thermoacoustic oscillations in a solid rocket motor,” *Exp. Therm. Fluid Sci.* **98**, 217–226 (2018).
- ³²L. Kabiraj, A. Saurabh, P. Wahi, and R. I. Sujith, “Route to chaos for combustion instability in ducted laminar premixed flames,” *Chaos* **22**(2), 023129 (2012).
- ³³Y. Guan, V. Gupta, and L. K. B. Li, “Intermittency route to self-excited chaotic thermoacoustic oscillations,” *J. Fluid Mech.* **894**, R3 (2020).
- ³⁴P. Kasthuri, I. Pavithran, S. A. Pawar, R. I. Sujith, R. Gejji, and W. Anderson, “Dynamical systems approach to study thermoacoustic transitions in a liquid rocket combustor,” *Chaos* **29**(10), 103115 (2019).
- ³⁵V. Nair, G. Thampi, and R. I. Sujith, “Intermittency route to thermoacoustic instability in turbulent combustors,” *J. Fluid Mech.* **756**, 470–487 (2014).
- ³⁶V. R. Unni and R. I. Sujith, “Flame dynamics during intermittency in a turbulent combustor,” *Proc. Combust. Inst.* **36**(3), 3791–3798 (2017).
- ³⁷H. Gotoda, Y. Shinoda, M. Kobayashi, Y. Okuno, and S. Tachibana, “Detection and control of combustion instability based on the concept of dynamical system theory,” *Phys. Rev. E* **89**(2), 022910 (2014).
- ³⁸C. Aoki, H. Gotoda, S. Yoshida, and S. Tachibana, “Dynamic behavior of intermittent combustion oscillations in a model rocket engine combustor,” *J. Appl. Phys.* **127**(22), 224903 (2020).

- ³⁹Y. Guan, L. K. B. Li, H. Jegal, and K. T. Kim, "Effect of flame response asymmetries on the modal patterns and collective states of a can-annular lean-premixed combustion system," *Proc. Combust. Inst.* **39**(4), 4731–4739 (2023).
- ⁴⁰T. Hashimoto, H. Shibuya, H. Gotoda, Y. Ohmichi, and S. Matsuyama, "Spatiotemporal dynamics and early detection of thermoacoustic combustion instability in a model rocket combustor," *Phys. Rev. E* **99**(3), 032208 (2019).
- ⁴¹S. Shima, K. Nakamura, H. Gotoda *et al.*, "Formation mechanism of high-frequency combustion oscillations in a model rocket engine combustor," *Phys. Fluids* **33**(7), 064108 (2021).
- ⁴²P. Kasthuri, A. Krishnan, R. Gejji, W. Anderson, N. Marwan, and R. I. Sujith, "Investigation into the coherence of flame intensity oscillations in a model multi-element rocket combustor using complex networks," *Phys. Fluids* **34**, 034107 (2022).
- ⁴³P. Kasthuri, S. A. Pawar, R. Gejji, W. Anderson, and R. I. Sujith, "Coupled interaction between acoustics and unsteady flame dynamics during the transition to thermoacoustic instability in a multi-element rocket combustor," *Combust. Flame* **240**, 112047 (2022).
- ⁴⁴Y. Liu, P. Liu, Z. Wang, W. Ao, G. Xu, and Y. Guan, "Numerical investigation of combustion instability in a liquid rocket engine: Interaction effect between hydrodynamics and acoustic mode," *Aerosp. Sci. Technol.* **143**, 108711 (2023).
- ⁴⁵Y. Liu, P. Liu, Z. Wang, W. Ao, and Y. Guan, "Numerical investigation of combustion instability in a single-element liquid rocket engine: Intermittency routes before and after thermoacoustic instability," *Aerosp. Sci. Technol.* **143**, 108691 (2023).
- ⁴⁶U. Bunge, C. Mockett, and F. Thiele, "Guidelines for implementing Detached-Eddy Simulation using different models," *Aerosp. Sci. Technol.* **11**(5), 376–385 (2007).
- ⁴⁷S. Iavarone, A. Péquin, Z. X. Chen, N. A. K. Doan, N. Swaminathan, and A. Parente, "An a priori assessment of the Partially Stirred Reactor (PaSR) model for MILD combustion," *Proc. Combust. Inst.* **38**(4), 5403–5414 (2021).
- ⁴⁸X. Han, J. Li, and A. S. Morgans, "Prediction of combustion instability limit cycle oscillations by combining flame describing function simulations with a thermoacoustic network model," *Combust. Flame* **162**(10), 3632–3647 (2015).
- ⁴⁹L. Selle *et al.*, "Compressible large eddy simulation of turbulent combustion in complex geometry on unstructured meshes," *Combust. Flame* **137**(4), 489–505 (2004).
- ⁵⁰Y. Sun, D. Zhao, C. Ji, T. Zhu, Z. Rao, and B. Wang, "Large-eddy simulations of self-excited thermoacoustic instability in a premixed swirling combustor with an outlet nozzle," *Phys. Fluids* **34**(4), 044112 (2022).
- ⁵¹See www.openfoam.org/ for "The OpenFOAM Foundation" (2013).
- ⁵²J. Li, Y. Xia, A. S. Morgans, and X. Han, "Numerical prediction of combustion instability limit cycle oscillations for a combustor with a long flame," *Combust. Flame* **185**, 28–43 (2017).
- ⁵³Y. Liu, P. Liu, Z. Wang, G. Xu, and B. Jin, "Numerical investigation of mode competition and cooperation on the combustion instability in a non-premixed combustor," *Acta Astronaut.* **198**, 271–285 (2022).
- ⁵⁴Y. Yalcinkaya and A. G. Gungor, "Pressure gradient effect on flame-vortex interaction in lean premixed bluff-body stabilized flames," *Phys. Fluids* **35**, 045105 (2023).
- ⁵⁵B. Wu, X. Zhao, B. R. Chowdhury, B. M. Cetegen, C. Xu, and T. Lu, "A numerical investigation of the flame structure and blowoff characteristics of a bluff-body stabilized turbulent premixed flame," *Combust. Flame* **202**, 376–393 (2019).
- ⁵⁶J. S. Hardi, W. Zach Hallum, C. Huang, and W. E. Anderson, "Approaches for comparing numerical simulation of combustion instability and flame imaging," *J. Propul. Power* **32**(2), 279–294 (2016).
- ⁵⁷W. E. Anderson and V. Yang, *Liquid Rocket Engine Combustion Instability* (NASA, 1995).
- ⁵⁸K. C. Schadow, E. Gutmark, T. P. Parr, D. M. Parr, K. J. Wilson, and J. E. Crump, "Large-scale coherent structures as drivers of combustion instability," *Combust. Sci. Technol.* **64**(4–6), 167–186 (1989).
- ⁵⁹K. C. Schadow and E. Gutmark, "Combustion instability related to vortex shedding in dump combustors and their passive control," *Prog. Energy Combust. Sci.* **18**(2), 117–132 (1992).
- ⁶⁰D. Huang, J. Xu, R. Chen, and H. Meng, "Large eddy simulations of turbulent combustion of kerosene-air in a dual swirl gas turbine model combustor at high pressures," *Fuel* **282**, 118820 (2020).
- ⁶¹K. Balasubramanian and R. I. Sujith, "Non-normality and nonlinearity in combustion-acoustic interaction in diffusion flames," *J. Fluid Mech.* **594**, 29–57 (2008).
- ⁶²A. Roy, C. P. Premchand, M. Raghunathan, A. Krishnan, V. Nair, and R. I. Sujith, "Critical region in the spatiotemporal dynamics of a turbulent thermoacoustic system and smart passive control," *Combust. Flame* **226**, 274–284 (2021).
- ⁶³D. A. Rosenberg, P. M. Allison, and J. F. Driscoll, "Flame index and its statistical properties measured to understand partially premixed turbulent combustion," *Combust. Flame* **162**(7), 2808–2822 (2015).